BRNO UNIVERSITY OF TECHNOLOGY

VYSOKÉ UČENÍ TECHNICKÉ V BRNĚ

FACULTY OF ELECTRICAL ENGINEERING AND COMMUNICATION

FAKULTA ELEKTROTECHNIKY
A KOMUNIKAČNÍCH TECHNOLOGIÍ

DEPARTMENT OF CONTROL AND INSTRUMENTATION

ÚSTAV AUTOMATIZACE A MĚŘICÍ TECHNIKY

HIGH POWER-EFFICIENT SENSORLESS CONTROL OF SYNCHRONOUS RELUCTANCE MOTOR

BEZSNÍMAČOVÉ ŘÍZENÍ SYNCHRONNÍHO RELUKTANČNÍHO MOTORU SE ZAMĚŘENÍM NA VYSOKOU ÚČINNOST

DOCTORAL THESIS STATEMENT

TEZE DIZERTAČNÍ PRÁCE

AUTHOR — Ing. Zbyněk Mynář
AUTOR PRÁCE

SUPERVISOR — prof. Ing. Pavel Václavek, Ph.D.
ŠKOLITEL

BRNO 2022

KEYWORDS
Synchronous, SynRM, Reluctance, FOC, Power optimization, MTPA, ME, EKF

KLÍČOVÁ SLOVA
Synchronní, SynRM, Reluktance, FOC, Optimalizace výkonu, MTPA, ME, EKF

MYNÁŘ, Z. *High power-efficient sensorless control of synchronous reluctance motor.* Brno, 2022, 48 p. Doctoral thesis statement. Brno University of Technology, Faculty of Electrical Engineering and Communication, Department of Control and Instrumentation. Advised by prof. Ing. Pavel Václavek, Ph.D.

Contents

Introduction

Synchronous reluctance motor (SynRM) is known since the first half of 20^{th} century [Kos23]. Thanks to technological advances in the design of SynRM rotors, which greatly enhanced machine performance, more and more attention is started to be paid to SynRM. The most notable advantages of this technology are:

- SynRM can achieve around 10% to 15% larger rated torque for a given frame size in comparison to an AC induction machine (ACIM) [BP08].
- Very low production cost because the assembly of laminated rotor topology is quite simple and requires no costly permanent magnets [MDD+22].
- There are no Joule losses in the rotor of SynRM. Resulting lower operation temperature has many benefits, like, for example, longer life of ball-bearings and reduced thermal requirements for lubricants [RFC10].
- There is no risk of permanent magnet demagnetization due to heat like in the case of permanent magnet synchronous machine (PMSM).
- Constant power region during field weakening can be theoretically extended to infinite speed because there is no permanent magnet flux to suppress.

It can be expected, that the low maintenance, production, and operation cost of SynRM will make it popular in cost-sensitive inverter-based applications like pumps, fans, or HVACs [BP08]. To fully exploit this potential, great attention is currently being paid to the development of power-optimal sensorless control algorithms for SynRM, which would minimize necessary operation input power and remove a need for expensive rotor position and speed sensor. The main complications of its power-efficient sensorless control are the major non-linearities of SynRM, specifically the magnetic saturation phenomenon and the core losses.

Power-optimal control is also the topic of this thesis, or more precisely, a proposal of sensorless state and parameter observer necessary to build such application. In its core, this thesis presents three key algorithms:

- An observer based on the extended Kalman filter combining independent measurements and models to achieve redundancy in rotor position information.
- Novel low-cost current derivative measurement method.
- Pulse-width modulation technique with improved power efficiency.

As will be shown by both simulations and experiments, these algorithms offer several attractive features, like full-speed operation range, improved efficiency, and the machine rotor and position information redundancy, which can be used to estimate additional machine states and parameters (this thesis shows an example with stator resistance estimation).

1. SynRM Model and Properties

The goal of this chapter is to introduce the SynRM non-linear system model and properties to show challenges related to its optimal control and to serve as a foundation for later chapters of this thesis.

1.1. Mathematical Model

The stator of SynRM is identical to a standard AC induction machine. The rotor, however, contains no windings or permanent magnets. It is constructed so the highest possible difference in magnetic reluctance is achieved between the rotor axes (and thus stator inductance as well). The rotor and stator always have the same number of pole pairs. When such a rotor is exposed to a rotating magnetic field, a torque is produced, because the most magnetically conductive rotor axis tries to align itself with the vector of the stator magnetic field. Such alignment achieves a minimal magnetic flux density in the air gap and with it a minimal energy state of the magnetic field.

Figure 1.1 depicts the typical construction topologies of the four-pole SynRM rotor. The most widespread rotor topology today is the transversally-laminated rotor as shown in Figure 1.1c. These rotors offer a relatively good balance between production cost and the maximal achievable torque [Kol10, ODM15].

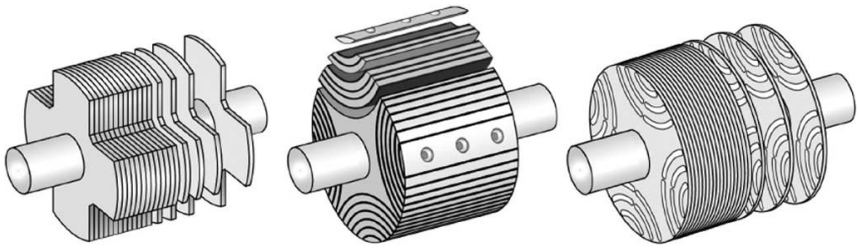

Figure 1.1: Rotor construction (a) with pronounced poles, (b) axially-laminated (c) transversally-laminated [Kol10]

Clarke's transformation will be used as the first step to obtain a sufficiently simple SynRM mathematical mode. The stator phase voltage vector $\vec{u}_{abc} = [u_a, u_b, u_c]^{\mathrm{T}}$ can be transformed as

$$\vec{u}_{\alpha\beta} = \begin{bmatrix} u_\alpha \\ u_\beta \end{bmatrix} = \frac{2}{3} \begin{bmatrix} 1 & -\frac{1}{2} & -\frac{1}{2} \\ 0 & \frac{\sqrt{3}}{2} & -\frac{\sqrt{3}}{2} \end{bmatrix} \vec{u}_{abc} = \mathbf{T}^{abc}_{\alpha\beta} \vec{u}_{abc}, \tag{1.1}$$

where $\vec{u}_{\alpha\beta}$ is the stator voltage vector in $\alpha\beta$ coordinate system and $\mathbf{T}^{abc}_{\alpha\beta}$ is Clarke's transformation matrix. The $\frac{2}{3}$ coefficient in equation (1.1) was added to normalize amplitudes of quantities in $\alpha\beta$ coordinate system with phase quantities [CČerný10].

Further model simplification can be achieved via Park's transformation, which converts quantities from the two-phase stationary $\alpha\beta$ to the two-phase rotating dq

coordinate system. The d axis is usually referred to as the direct axis and the q axis as the quadrature axis. The SynRM stator voltage vector can be written as

$$\vec{u}_{dq} = \begin{bmatrix} u_d \\ u_q \end{bmatrix} = \mathbf{T}_{dq}^{\alpha\beta}(\theta_e) \begin{bmatrix} u_\alpha \\ u_\beta \end{bmatrix} = \begin{bmatrix} \cos\theta_e & \sin\theta_e \\ -\sin\theta_e & \cos\theta_e \end{bmatrix} \vec{u}_{\alpha\beta}, \tag{1.2}$$

where $\vec{u}_{dq}$ is the stator voltage vector in dq coordinate system, θ_e is the rotation angle, and $\mathbf{T}_{dq}^{\alpha\beta}(\theta_e)$ is the Park's transformation matrix.

The electrical angle θ_e is chosen with regard to the simplicity of the resulting mathematical model. In this work, similarly to majority of literature, alignment of d-axis with the maximal inductance axis will be used [CČerný10, ITDO06].

The stator voltage in stationary reference frame can be described by equation

$$\vec{u}_{\alpha\beta} = R_s \vec{i}_{\alpha\beta} + \mathrm{d}\vec{\Psi}_{\alpha\beta}/\mathrm{d}t, \tag{1.3}$$

where R_s is stator winding resistance, $\vec{i}_{\alpha\beta} = [i_\alpha, i_\beta]^{\mathrm{T}}$ is stator current vector and $\vec{\Psi}_{\alpha\beta} = [\Psi_\alpha, \Psi_\beta]^{\mathrm{T}}$ is stator magnetic flux vector in $\alpha\beta$ reference frame. Equation (1.3) can be expressed in rotating reference frame as

$$\vec{u}_{dq} = R_s \vec{i}_{dq} + \omega_e \begin{bmatrix} 0 & -1 \\ 1 & 0 \end{bmatrix} \vec{\Psi}_{dq} + \frac{\mathrm{d}}{\mathrm{d}t}\vec{\Psi}_{dq} = R_s \vec{i}_{dq} + \omega_e \mathbf{Z}\vec{\Psi}_{dq} + \frac{\mathrm{d}}{\mathrm{d}t}\vec{\Psi}_{dq}, \tag{1.4}$$

where $\omega_e = \mathrm{d}\theta_e/\mathrm{d}t$ is synchronous electrical speed, $\mathbf{Z}$ is $\pi/2$ rotation angle matrix, $\vec{i}_{dq} = [i_d, i_q]^{\mathrm{T}}$ is stator current vector, and $\vec{\Psi}_{dq} = [\Psi_d, \Psi_q]^{\mathrm{T}}$ is magnetic flux vector.

One of the SynRM disadvantages, which complicate its control, is non-linearity of the magnetic circuit, which saturates even with nominal currents. An ideal direct axis flux is depicted in Figure 1.2a and the real saturating flux in Figure 1.2b.

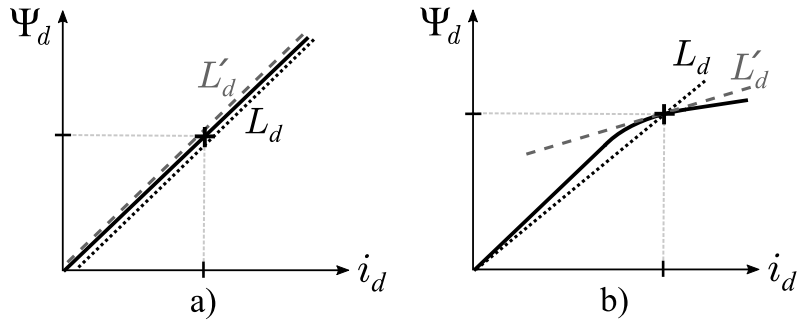

Figure 1.2: Stator magnetic flux a) with and b) without saturation [ITDO06]

The stator magnetic flux considering the saturation effect can be described as

$$\vec{\Psi}_{dq} = \begin{bmatrix} L_d(i_d) & 0 \\ 0 & L_q(i_q) \end{bmatrix} \vec{i}_{dq} = \mathbf{L}\vec{i}_{dq}, \tag{1.5}$$

where $\mathbf{L}$ is the static inductance matrix, $L_d(i_d)$ is the static inductance in the direct axis, and $L_q(i_q)$ in the quadrature axis. Static inductances are given by the ratio between the magnetic flux and the current amplitudes. To accurately describe dynamic events, the dynamic inductances $L'_d(i_d)$ and $L'_q(i_q)$, which can be interpreted as tangent to flux characteristics in the operation point, can be introduced into the

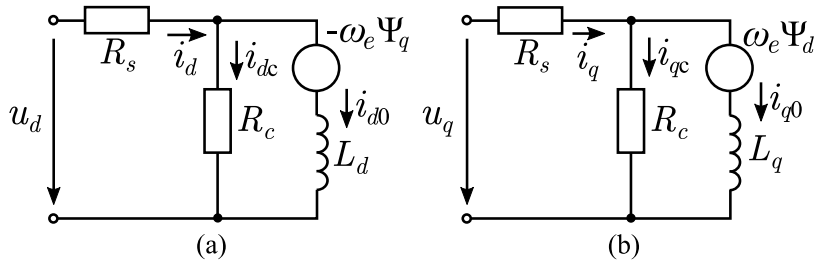

Figure 1.3: The SynRM model with core losses in a) direct and b) quadratic axis

model [ITDO06, XXLN91]. Note that from now on, both the static and dynamic inductances will be stated without their explicit current dependency.

The SynRM machine core-losses P_{Fe} were neglected up until this moment. These are formed by magnetization as hysteresis losses and represent the second most significant losses after the Joule losses. The P_{Fe} are usually modelled using the resistance R_c. The resulting SynRM model is shown in Figure 1.3. It can be noticed that the measured current $\vec{i}_{dq}$ is now divided into loss current $\vec{i}_{dqc} = [i_{dc}, i_{qc}]^{\mathrm{T}}$ and flux-producing current $\vec{i}_{dq0} = [i_{d0}, i_{q0}]^{\mathrm{T}}$. Only the steady-state was considered to obtain a simple model, which can be afforded if the SynRM is used in low-dynamic applications. The inclusion of core loss resistance R_c into the model benefits the accuracy of found solution. The voltage equations (1.4) can be rewritten as

$$\vec{u}_{dq} = R_s \vec{i}_{dq0} + \mathbf{L}' \frac{\mathrm{d}}{\mathrm{d}t} \vec{i}_{dq0} + \omega_e \left(1 + \frac{R_s}{R_c}\right) \mathbf{L}\mathbf{Z} \vec{i}_{dq0}, \tag{1.6}$$

where $\mathbf{L}'$ is the dynamic inductance matrix [IKK+09, KS96, XXLN91].

Electrical torque applied to the machine shaft can be calculated as

$$T_e = \frac{3}{2} P_p (\vec{\Psi}_{dq} \times \vec{i}_{dq0}) = \frac{3}{4} P_p (L_d - L_q) I_{m0} \sin 2\theta_{I0}, \tag{1.7}$$

where P_p is the number of pole pairs. It can be seen that the difference between d and q axis inductances is critical for achieving high torque.

To make the mathematical model complete, the mechanical equation

$$\frac{\mathrm{d}\omega_m}{\mathrm{d}t} = \frac{1}{J} \left[T_e - T_l - B_1 \omega_m - \mathrm{sign}(\omega_m) B_2 \omega_m^2 \right] \tag{1.8}$$

is introduced, where $\omega_m = \omega_e / P_p$ is mechanical rotor speed, J is the moment of inertia, T_l is the loading torque, B_1 is internal machine viscous friction coefficient and B_2 is a ventilator mechanical loss coefficient. The rotor electrical position is

$$\theta_e = \int \omega_e \mathrm{d}t. \tag{1.9}$$

In summary, the final mathematical model of SynRM, including magnetic saturation and core losses, is formed by equations (1.6), (1.8), and (1.9) [CČerný10].

1.2. Parameters of Real SynRM Machine

This section will be discussing the offline-measured parameters of real SynRM with the goal to highlight the extent of parameter non-linearities of real machine. The investigated machine is 550 W SynRM with transversally-laminated rotor (as shown in Figure 1.1c) from the KSB manufacturer. It was also used as reference machine in this thesis. Its basic parameters are listed in Table 1.1 and in Figure 1.4. The stator resistance R_s was measured using the RLC meter and the mechanical parameters J and B were acquired from step dynamic response.

Table 1.1: Reference SynRM parameters

Quantity	Value	Unit
P_{nom}	550	W
N_{nom}	1500	rpm
U_{nom}	350	V_{rms}
I_{nom}	1.6	A_{rms}
P_p	2	-
R_s	9.68	Ω
J	$1.64 \cdot 10^{-3}$	$\text{kg} \cdot \text{m}^2$
B	$1.96 \cdot 10^{-3}$	$\text{Nm} \cdot \text{s/rad}$

Figure 1.4: Reference SynRM label

The stator inductances were acquired using locked-rotor offline measurement, a simple stator flux model (1.3), and multi-linear regression method (MLR) [BCP16]. The acquired static inductances are in Figure 1.5 and Figure 1.6. The L_d is several times higher than L_q and also saturates at much higher currents. This was expected because the d rotor axis is in majority formed by iron, while the q axis is air-dominant. The q axis path, therefore, saturated with a small current (see Figure 1.6, where the L_q drops to 25 % when $|i_q| > 0.5$ A). Some published SynRM control algorithms consider L_q to be constant for simplicity [HKS99, KSG+14]. The measurement shows that this simplification is true only with sufficient stator current amplitude. Figure 1.5 shows that the L_d drops by one-third at nominal stator current I_{nom}. This effect cannot be neglected for efficiency-optimal sensorless SynRM control. In comparison, the cross-saturation effect is relatively negligible.

The core-loss modelling resistance R_c characteristics in Figure 1.7 was acquired from core power loss estimation, which was determined as a difference between the measured machine input electrical power, output mechanical power, estimated Joule losses, and internal mechanical stator losses. Note that the missing map area for high speed and flux products could not be measured due to stator voltage limitation. The SynRM model equation (1.6) is impacted by the ratio between R_c and R_s. It can be noticed that R_c can differ significantly based on the actual operating point, however, in general, the R_c is several hundred times higher than stator resistance R_s for all measured operation points. It can, therefore, be assumed, that accurate modelling of the non-linearity caused by saturation is going to have a higher impact on SynRM model accuracy than core losses.

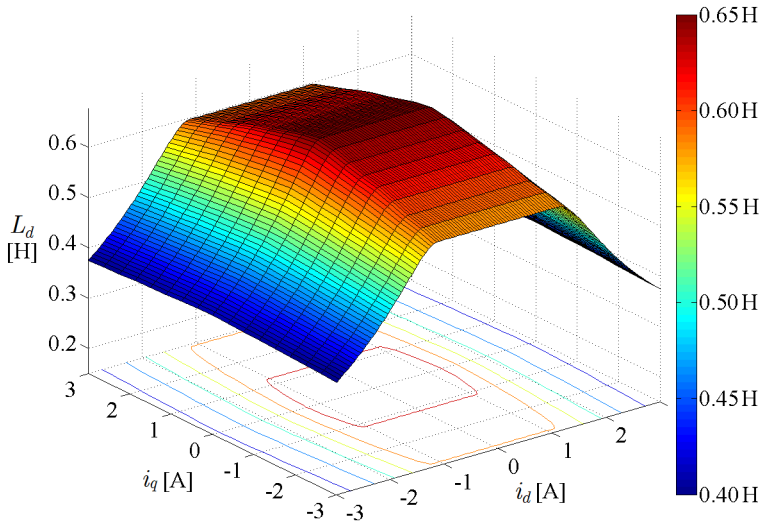

Figure 1.5: Direct axis static inductance L_d dependency on stator current $\vec{i}_{dq}$

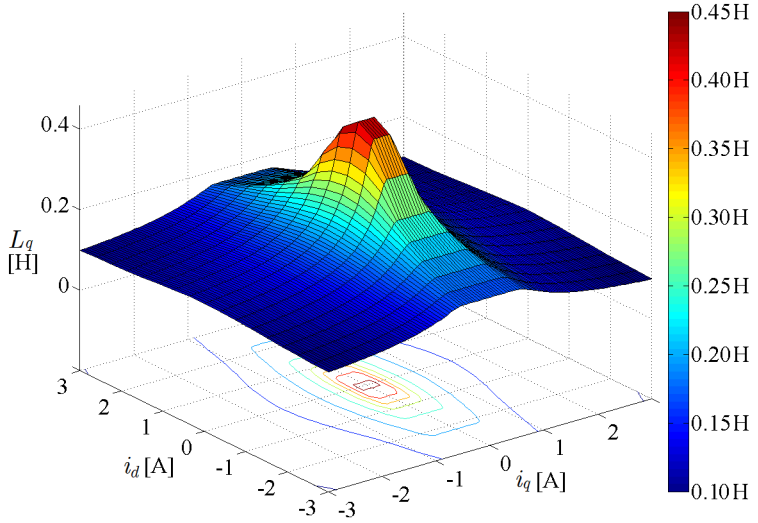

Figure 1.6: Quadrature axis static inductance L_q dependency on stator current $\vec{i}_{dq}$

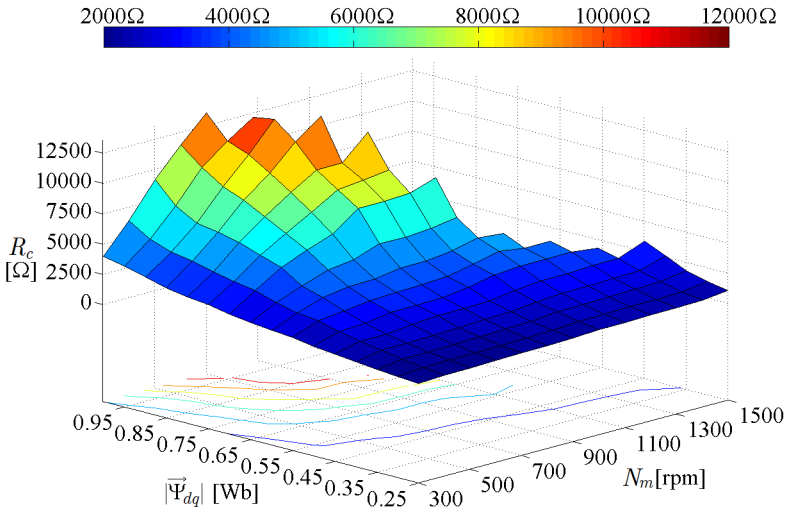

Figure 1.7: Resistance R_c dependency on stator flux $|\vec{\Psi}_{dq}|$ and the speed N_m

2. SynRM Sensorless Control

This thesis focuses on field-oriented control algorithms, which are very similar to the FOC of the interior permanent magnet synchronous motors [XXLN91]. As shown in Chapter 1, the harmonic voltages, currents, and fluxes within the rotor-aligned dq-axis frame are turned into DC quantities, which allows the FOC to control the machine stator flux and rotor torque by controlling dq-axis stator currents $\vec{i}_{dq}$ to

$$\vec{i}_{dq}^{\,\mathrm{req}} = \begin{bmatrix} i_d^{\mathrm{req}} \\ i_q^{\mathrm{req}} \end{bmatrix} = I_m^{\mathrm{req}} \begin{bmatrix} \cos\theta_I^{\mathrm{req}} \\ \sin\theta_I^{\mathrm{req}} \end{bmatrix}, \tag{2.1}$$

where I_m^{req} is the amplitude and θ_I^{req} is the angle of stator current reference. As will be discussed later, the θ_I^{req} angle directly affects the efficiency of SynRM operation.

High-level block diagram of the most common form of the FOC algorithm is shown in Figure 2.1. The stator current control loops are often based on direct and quadrature axis current PI-type controllers. The stator current references $\vec{i}_{dq}^{\,\mathrm{req}}$ are then set by the outer control loop or loops, which reflect the type of targeted application (e.g. whether the goal is the speed, position, or torque control).

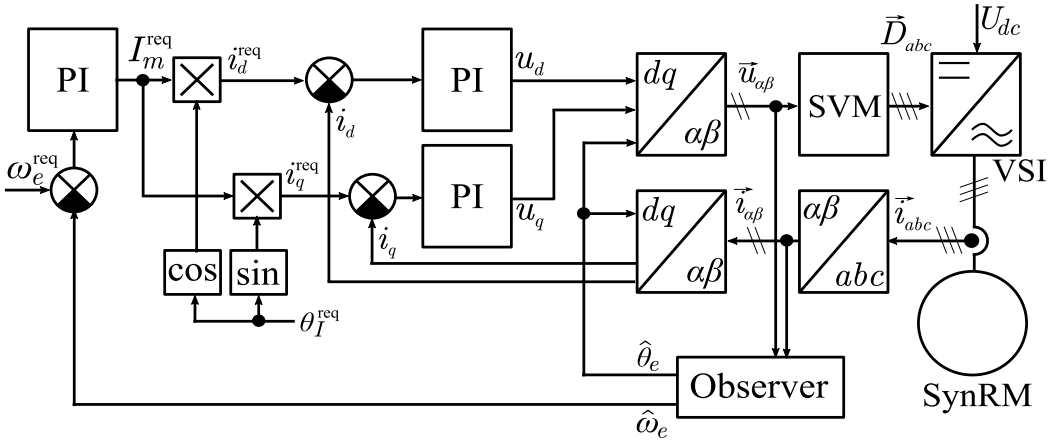

Figure 2.1: Generic block diagram of SynRM sensorless vector control

Such a PID-based cascaded control structure allows to build a high-performing drive system. That being said, alternatives are being proposed to bring further improvements. For example, the topic of model-based predictive control has been gaining attention in recent years, mainly because it allows straightforward and easy to understand tuning and constraint handling [Myn15,MVV16,VM17]. These methods are adopted slowly by industry mainly due to increased computational demands.

The stator voltages $\vec{u}_{\alpha\beta}$ are translated to phase duty-cycle control signals $\vec{D}_{abc}$ and then applied to the machine using the Voltage Source Inverter (VSI) power stage. A generic block diagram of three-phase VSI is shown in Figure 2.2. Number of methods for obtaining the inverter control signals AT, AB, BT, BB, CT, and CB exist [KC17]. A very common is the standard Space Vector Modulation (SVM), which principle is depicted in Figure 2.3. The two-state VSI can generate six active voltage vectors $\boldsymbol{v}_1$, $\boldsymbol{v}_2$, $\boldsymbol{v}_3$, $\boldsymbol{v}_4$, $\boldsymbol{v}_5$, and $\boldsymbol{v}_6$ and two zero voltage vectors $\boldsymbol{v}_0$ and $\boldsymbol{v}_7$. Their selection and calculation of their durations $T_{\boldsymbol{v}_0}$ up to $T_{\boldsymbol{v}_7}$ during the PWM

period T_{PWM} depends on the voltage vector $\vec{u}_{\alpha\beta}$ and corresponding SVM sector. An example of the centre-aligned PWM (CAPWM) scheme is shown in Figure 2.4.

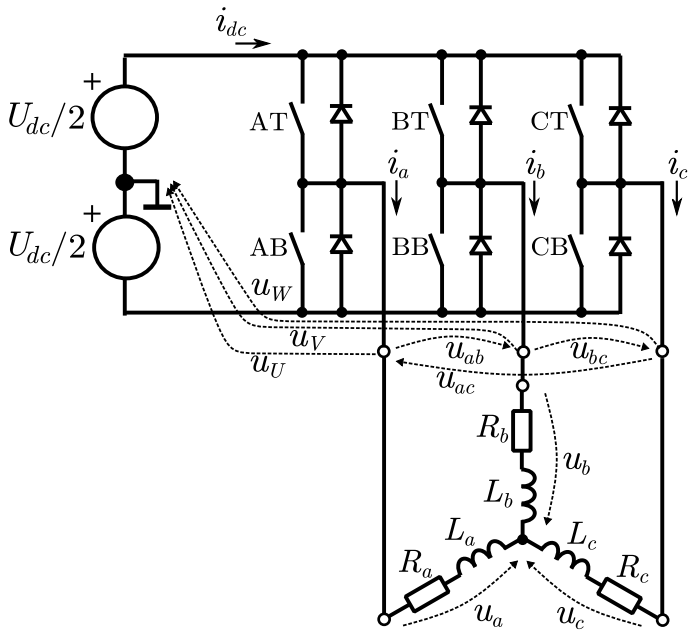

Figure 2.2: Block diagram of generic three-phase Voltage Source Inverter

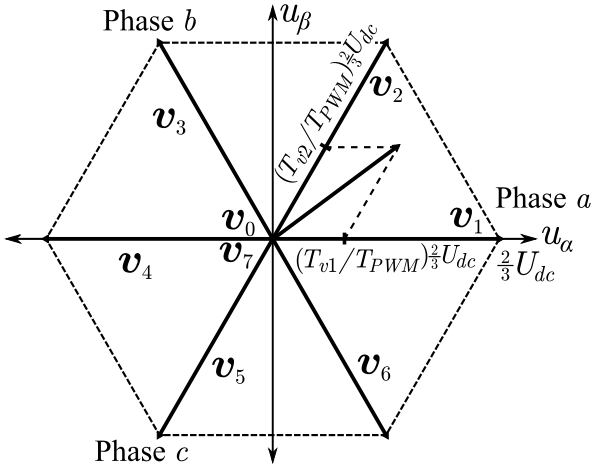

Inverter control signals

	AT	AB	BT	BB	CT	CB
$\boldsymbol{v}_0$	0	1	0	1	0	1
$\boldsymbol{v}_1$	1	0	0	1	0	1
$\boldsymbol{v}_2$	1	0	1	0	0	1
$\boldsymbol{v}_3$	0	1	1	0	0	1
$\boldsymbol{v}_4$	0	1	1	0	1	0
$\boldsymbol{v}_5$	0	1	0	1	1	0
$\boldsymbol{v}_6$	1	0	0	1	1	0
$\boldsymbol{v}_7$	1	0	1	0	1	0

Figure 2.3: Standard space vector modulation voltage generation [MVB21]

The rotor speed ω_e and especially the rotor position θ_e are critical for FOC. Both could be measured using a sensor. The drive realization without such sensor, however, leads to lower cost and improvement in reliability. This, together with the increasing capabilities of computation technology, lead to the development of sensorless algorithms, which can estimate these quantities. The SynRM sensorless estimation algorithms can be classified based on the utilized physical principle:

- The first class of algorithms utilizes the extended back-electromotive force (EEMF). These algorithms are using the machine model and require knowledge of actual machine parameters. The amplitude of EEMF voltage increases with the rotor speed and, therefore, these algorithms are suited for medium- to high-speed regions [TH14, ITDO06, VPF96].

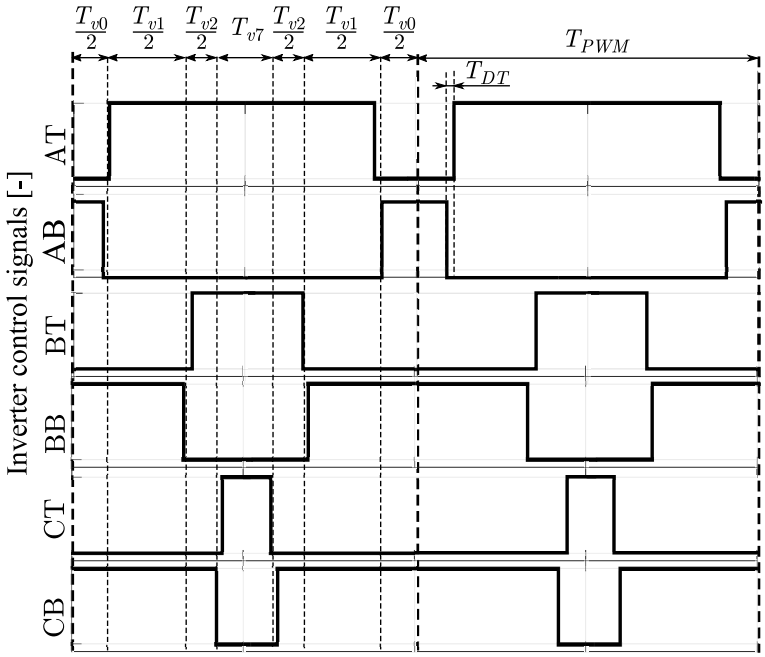

Figure 2.4: Example of the centre-aligned PWM waveform

- The second class covers the rotor saliency-based algorithms. Some such algorithms rely on high-frequency signal injection (HFI) into the fundamental control voltage or current. Demodulation of machine current then provides the rotor position information. The injected signal frequency upper limit is the inverter carrier PWM frequency and the bottom limit is given by the control algorithm frequency bandwidth (i.e. hundreds of Hertz to units of kHz). Other saliency-based algorithms (e.g. the well-known INFORM method) rely on excitation of stator currents by the fundamental phase PWM waveforms, but due to worse signal-to-noise ratio, it is often necessary to employ special current derivative measurement sensors. General advantage of all saliency-based algorithms are their ability to operate at low-speed and usually no need for exact knowledge of machine parameters [JSH+02, HNS17, NSS20].

- To exploit the advantages of both sensorless algorithm classes, hybrid algorithms were developed. The saliency-based principle is then usually used at a standstill and low speed and with the increasing speed, the estimation is transitioned to EEMF-based algorithm [KSG+14, TH14].

The performance and stability of the sensorless algorithms may be affected due to SynRM non-linearity, parameter spread from manufacturing, machine heating, and wear and tear. This brings the topic of online parameter estimation and adaptivity. A well-known approach is, for example, combination of the EEMF observer with loop-up table (LUT) of offline-measured parameters or with the Recursive Least-Square (RLS) online estimation algorithm [ITDO06, Tuo14, YAA09].

3. Efficiency Optimization

The input electrical power P_{in} is distributed within SynRM into Joule power loss P_{Cu} in the stator winding, core power loss P_{Fe}, internal mechanical power loss P_{ω}, and the mechanical output power applied to the shaft. When compared with a similar IE4 induction machine, the overall Joule losses are comparable in size but are all focused in the stator. The P_{Fe} and P_{ω} losses are usually similar in size as well. To give an idea of a typical SynRM nominal loss distribution, it was reported that for a four-pole 2.2 kW SynRM with 90 % nominal efficiency, the Joule losses contributed by 7.8 %, core losses by 1.7 %, and mechanical power losses by 0.5 % [JZL+19].

A SynRM electrical power loss minimization problem is performed via optimization of the current angle θ_I^{req} (see Figure 2.1). There is always one power loss global minimum. This can be seen in Figure 3.1, which was simulated for SynRM described in Section 1.2. The two well-known criteria of SynRM power optimality:

- The first criterion is the *Max Torque Per Ampere* (MTPA), which lies in the minimization of the stator current for a given torque, thus, minimizing Joule losses P_{Cu}. The MTPA law can be expressed from torque equation (1.7) as

$$\mathrm{d}T_e/\mathrm{d}\theta_I = 0.75 P_p I_m^2 (L_d - L_q) \cos 2\theta_I = 0 \text{ Nm/rad}, \tag{3.1}$$

  where the optimal operating point θ_I corresponds to minimal current I_m. Equation (3.1) would suggest solution $\theta_I = \pi/4$, however, the saturation effect makes the trajectory non-linear. Because the torque is proportional to $L_d - L_q$ difference, it is beneficial to saturate the q-axis but avoid d-axis saturation, always leading to current angle $\theta_I > \pi/4$ (see Figure 3.2).

- The second criterion is the *Maximum Efficiency* (ME) operation, which minimizes both Joule losses P_{Cu} and core losses P_{Fe}. Inclusion of core losses generally increases the optimal current angle (see Figure 3.2) because the core losses P_{Fe} are decreasing with stator flux vector amplitude $|\vec{\Psi}_{dq}|$.

Beside the machine power losses, the inverter operation can be optimized as well. Power losses in inverter semiconductors can be generally described as a sum of conductive power losses P_{con} and switching power losses P_{sw}. For IGBT-based VSI (shown in Figure 2.2), the overall losses increase with phase current amplitude [Sem12, Sem14, RK20]. This moves the ME trajectory towards the MTPA curve, as shown in Figure 3.2.

Power optimization algorithms in the literature can be classified into two groups:

- The first class are the *Loss-Model Controllers* (LMC), which are based on knowledge of the machine parameters and power loss model. Typical properties of LMC algorithm are quick convergence at the cost of sensitivity to machine parameter and model accuracy. Probably the most well-known LMC algorithm is the constant $\theta_I = \pi/4$ angle setup (i.e. MTPA rule for ideal SynRM). When including the saturation effect, LMC algorithms become more complex, often leading numerical solutions. An exception would be the often-used look-up table (LUT) with offline-measured optimal trajectory of current angle [QH13, YAA09, FZYJ20].

- The second class are the *Search Controllers* (SC), which involve an active search of the optimal operating point based on the measured input power. While the SC algorithms do not require previous knowledge of machine parameters, their convergence time is usually slower and their operation requires a signal injection or operating point sweep, causing torque ripple and related small efficiency drops. Depending on the character of the injected signal, SC algorithms can be further classified into algorithms with a discrete search step, continuous search, low-frequency injection, or high-frequency injection [DTCB22, QH13, BPPS10]. A variant of the MTPA search controller algorithm was also published as part of the research for this thesis. The DC current injection in the stator reference frame was employed, which allowed for algorithm simplification [Myn16].

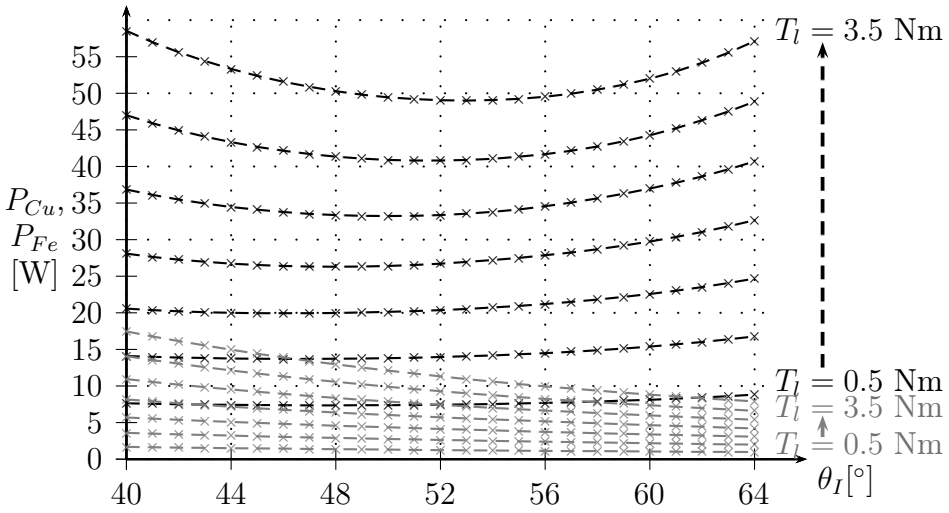

Figure 3.1: Simulated Joule losses P_{Cu} (black) and core losses P_{Fe} (grey) dependency on current angle θ_I and load T_l

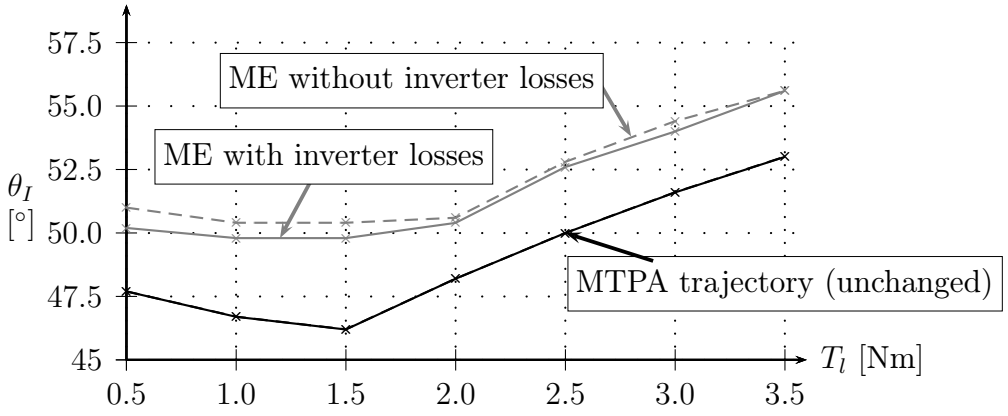

Figure 3.2: Simulated MTPA and ME trajectories for reference SynRM with semiconductor losses in reference FNB14560 IGBT module taken into account

4. Current State of SynRM Power-optimal Control

The SC algorithms shown in Section 3 are working very well in applications where the impact of change of current angle on the optimized quantity (i.e. stator current for MTPA or input power for ME criterion) can be evaluated. This means systems where load changes very slowly, often reaches prolonged states of steady-state, or follows defined cycles (e.g. pumps or fans). Taking into account relatively low computational demands and a natural adaptivity, the search-type algorithms were found to be quite mature and likely to be preferred in any suitable application. Therefore, these algorithms were not investigated further in this thesis.

The LMC algorithms can be used in a wider range of applications as they converge quickly and without need of detecting feedback to injected signal. An accurate solution can be obtained, however, such high performance has two conditions:

- Accurate machine parameters are provided to the LMC algorithm. The main causes of the current angle error $\theta_I^{\mathrm{err}} = \theta_I^{\mathrm{opt}} - \hat{\theta}_I$ are usually an inaccurate model of stator inductances, temperature drift, or manufacturing deviances.
- The machine control algorithm is operated with an accurate rotor position estimate $\hat{\theta}_e$. The position estimation error θ_e^{err} directly offsets the solution $\hat{\theta}_I$ found by the LMC algorithm. This increases performance requirements for position estimation algorithms (see Section 2), which are often also sensitive to accuracy of machine model and parameters.

The above topics were chosen as the main focus of this thesis. Simulations were done for the reference SynRM machine to evaluate sensitivity and necessary performance of typical LMC and position estimation algorithms (see Section 4.1 and Section 4.2). Finally, the exact goals of the thesis are summarized in Section 4.3.

4.1. Analysis of LMC Sensitivity to Machine Parameter and Position Errors

The sensitivity of machine power losses to position error $\theta_I^{\mathrm{err}} = \theta_e^{\mathrm{err}}$ was investigated by simulating difference of Joule and iron power-losses $\Delta(P_{Cu} + P_{Fe})$ to true ME trajectory in reaction to the position error. The results are in Figure 4.1. As expected, the power losses increase with position error, but the important outcome is that rate is non-linear and almost exponential. For purpose of this thesis, it will be further assumed that maximal steady-state $|\theta_e^{\mathrm{err}}|$ up to 7.5 degrees is acceptable (corresponds roughly to one percent efficiency loss).

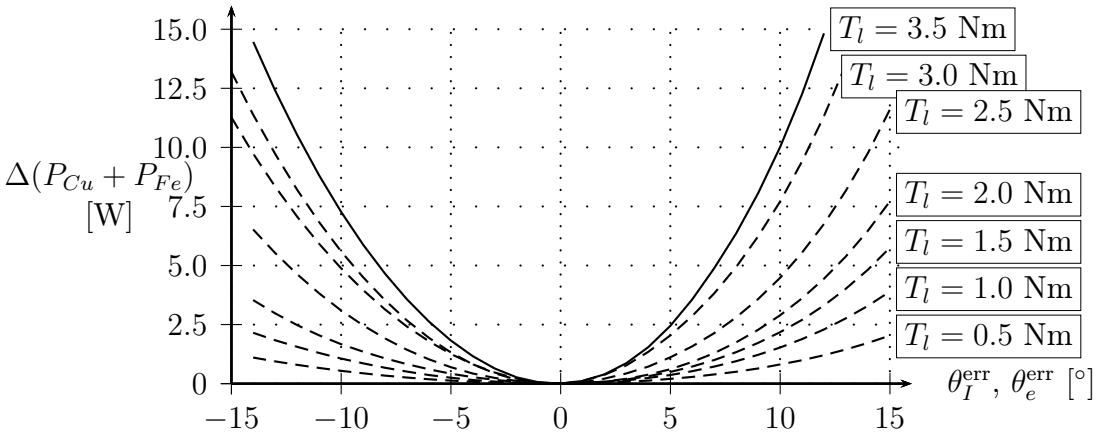

Figure 4.1: Simulated increase in SynRM power losses $\Delta(P_{Cu} + P_{Fe})$ versus the position estimate error θ_e^{err} at nominal speed

The second analysis investigated the sensitivity of the optimal LMC algorithm to error in stator inductance characteristics. The LMC performance was simulated with deformed characteristics $\hat{L}_d = k_d f_d(i_d/k_d, i_q/k_q)$ and $\hat{L}_q = k_q f_q(i_d/k_d, i_q/k_q)$ where k_d and k_q are dimensionless coefficients. Note that cases where condition $\hat{L}_q > \hat{L}_d$ occurred were not considered as valid. The results of simulation for reference SynRM running at nominal rotor speed $N_m = 1500$ rpm and a nominal rotor load $T_l = 3.5$ Nm are in Figure 4.2. When comparing the error θ_I^{err} to reference point $k_d = k_q = 1$, it can be seen that even for parameter errors around ±30 %, the previously discussed limit of 7.5 degrees is not violated. Hence deviations up to ±30 % are going to be seen as acceptable in this thesis. Similar results were obtained when simulating sensitivity to stator resistance estimate $\hat{R}_s$ error.

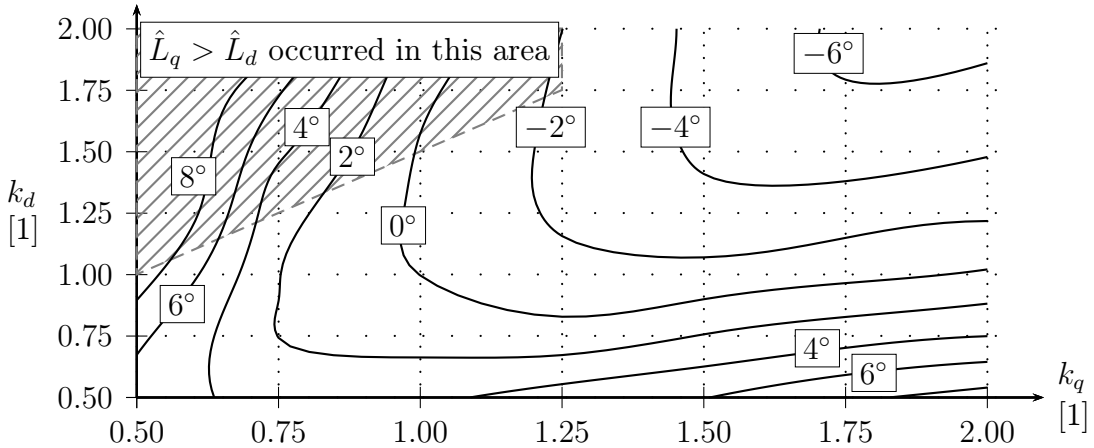

Figure 4.2: Simulated sensitivity of current angle θ_I^{err} of optimal LMC algorithm to inaccuracy of inductance $\hat{L}_d$ and $\hat{L}_q$ parameters

4.2. Evaluation of Position Estimator Sensitivity to Machine Parameter Error

The well-known combination of EEMF rotor position and RLS machine parameter estimation algorithms from Section 2 was investigated to gain a general idea of their machine parameter sensitivity. The EEMF observer, is mainly dependent on the $\hat{R}_s$, $\hat{L}_q$, and $\hat{L}'_d$ machine parameters, where the $\hat{L}'_d$ does not affect the steady-state performance. The simulated parameter sensitivity of the position estimate is in Figure 4.3. The sensitivity to δ_{R_s} is lower than to δ_{L_q} because the stator winding voltage drop is usually much smaller than the EMF voltage. In general, the overall sensitivity is similar to the ideal LMC algorithm simulated in Section 4.1.

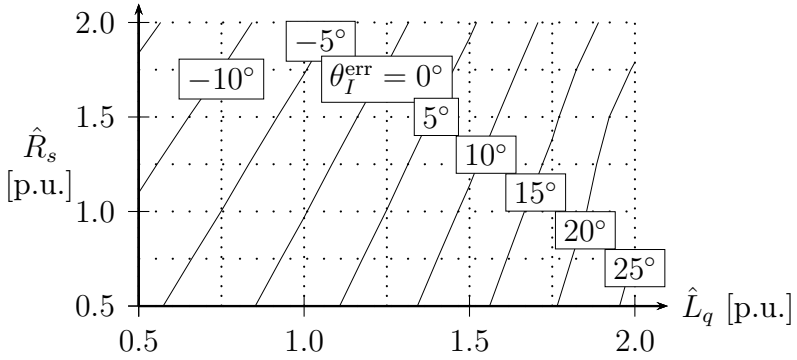

Figure 4.3: Sensitivity of the position estimate error $\hat{\theta}_e^{\mathrm{err}}$ of EEMF observer to error of inductance $\hat{L}_q$ and resistance $\hat{R}_s$

The online RLS algorithm was run on a real SynRM machine at the speed $N_m = 750$ rpm, $\theta_I = \pi/4$, and various loads to gain more realistic data. The experimental results are shown in Figure 4.4. The $\hat{L}_q$ and especially the $\hat{R}_s$ estimates reach errors in tens of percent, which is a similar performance as in the original EEMF and RLS publication [ITDO06]. This indicates that a high parameter estimation accuracy, which would safely ensure a small position estimation error $\hat{\theta}_e^{\mathrm{err}}$ (i.e. the ±30 % limit), is not a trivial matter and requires special consideration.

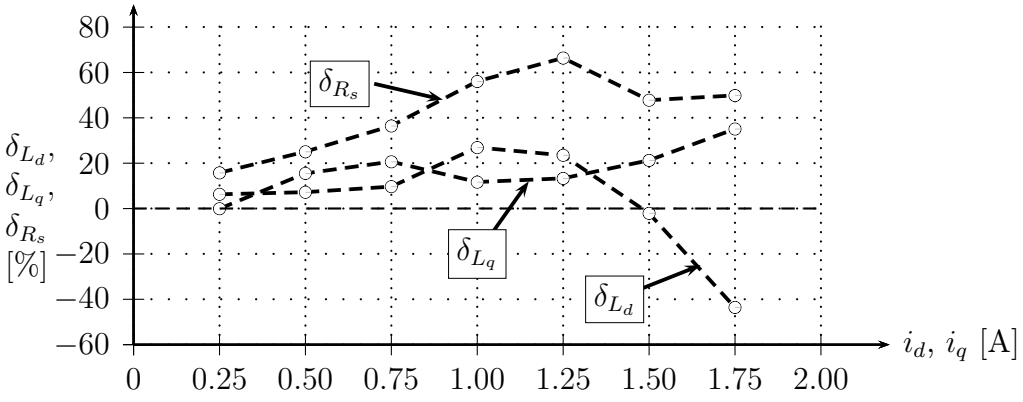

Figure 4.4: Estimated parameter errors δ_{L_d}, δ_{L_q}, and δ_{R_s} in relative values

4.3. Goals of the Thesis

Based on the discussion in previous sections, it was determined that a rotor position and motor parameter estimator, which would support the operation of the LMC power-optimization algorithm should be pursued within this thesis. The desired algorithm placed within the FOC block diagram is shown in Figure 4.5. As a summary, the following traits should be achieved:

1. The steady-state position estimate error θ_e^{err} should be below 7.5 degrees, but as small as possible in general. This should be achieved in all load and speed regions. It can be expected, that a robust adaptation to the change of the inductances in both axes will be necessary.

2. The machine parameter estimates should be provided to other algorithms within the FOC structure. This regards especially the stator inductances because their acquisition is not a trivial matter. Accuracy within the ±30 % range is acceptable, provided that position error θ_e^{err} is not affected.

3. The convergence to the optimal θ_I^{opt} operating point should not require signal injection, which would limit the applicability of the algorithm. This is necessary because the injection is the main limitation of SC algorithms, which are otherwise preferable.

4. The algorithm should require no or inexpensive additional hardware.

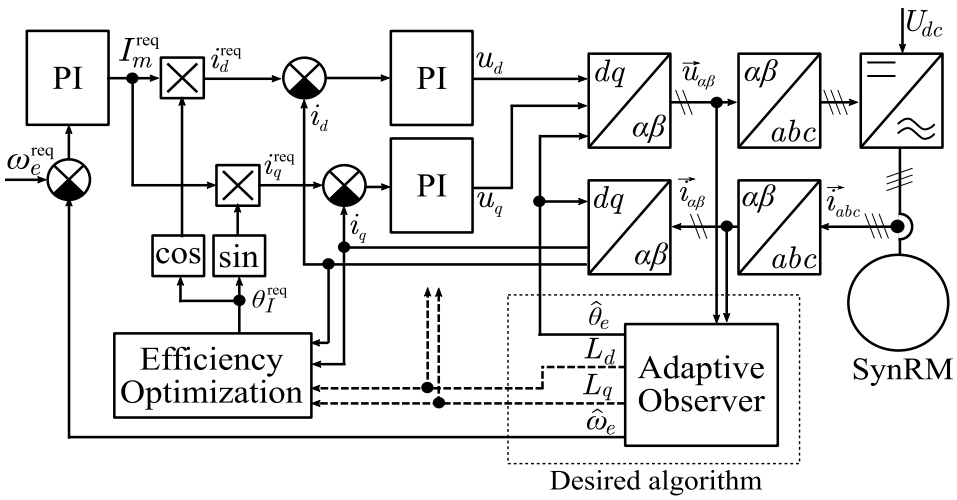

Figure 4.5: Block diagram of desired sensorless estimation algorithm within FOC structure

5. Proposed Sensorless Adaptive Estimation Method

This chapter presents algorithms, which were developed during research for this thesis as an answer to goals defined in Chapter 4. The saliency-based algorithms with a fundamental pulse width modulation (PWM) excitation and stator current derivative measurement were found to be promising for further research. It was shown by other authors that it is possible to simultaneously estimate stator inductances, position, and speed [RSW19]. The research of this thesis, therefore, focused on the further development of this idea. The block diagram of FOC with LMC-type optimization and newly proposed algorithms (highlighted in grey colour) is in Figure 5.1. The proposed algorithms are:

- *The current derivative measurement method* (see MC IDC and reluctance measurement blocks in Figure 5.1). The method is described in Section 5.1.
- *The alignment-swap PWM switching scheme.* See details in Section 5.2.
- *The extended Kalman filter utilizing measurement redundancy.* Two variants of this algorithm are presented and in Section 5.4.

Note that the core of the proposed method was already published, however, this thesis presents a number of modifications [MVB21].

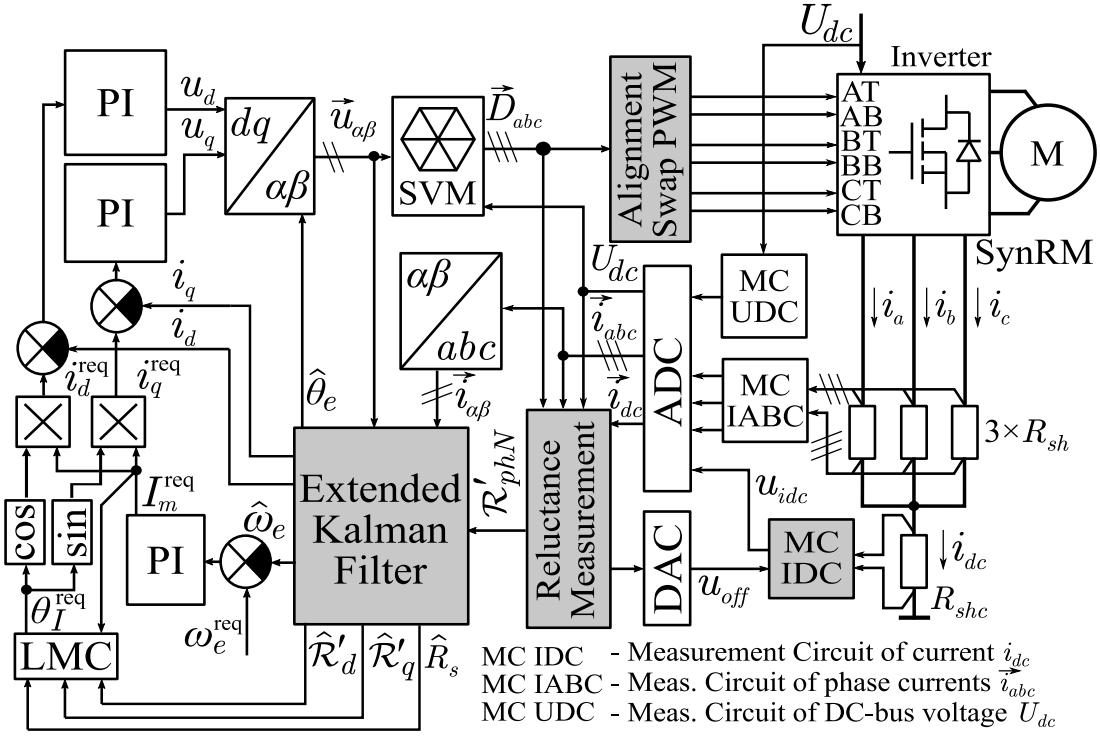

Figure 5.1: Block diagram of vector control using the proposed algorithm (newly proposed elements in grey) [MVB21]

5.1. Method of Obtaining Rotor Position from Current Derivative Measurements

The SynRM inductances L_a, L_b, and L_c in motor phases $N \in \{a, b, c\}$ are affected by the rotor position θ_e. The VSI, as depicted in Figure 2.2, applies six non-zero SVM voltage vectors $\boldsymbol{v}_M = \{\boldsymbol{v}_1, \boldsymbol{v}_2, \boldsymbol{v}_3, \boldsymbol{v}_4, \boldsymbol{v}_5, \boldsymbol{v}_6\}$ for the duration $\boldsymbol{T}_{vM} = \{T_{v1}, T_{v2}, T_{v3}, T_{v4}, T_{v5}, T_{v6}\}$. Example of the resulting RL circuits for $\boldsymbol{v}_1$ and $\boldsymbol{v}_4$ are shown in Figure 5.2.

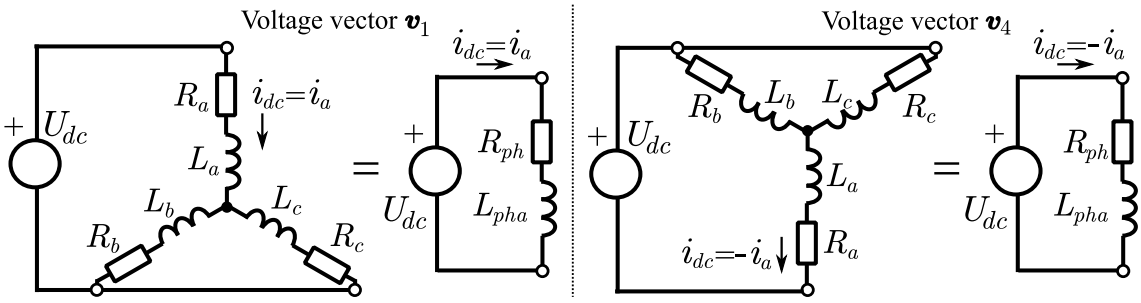

Figure 5.2: Equivalent circuits for voltage vectors $\boldsymbol{v}_1$ and $\boldsymbol{v}_4$

The normalized reluctance $\mathcal{R}'_{phN}$ quantity is introduced next as

$$\mathcal{R}'_{pha} = \frac{3}{2}\frac{1}{L_{pha}} = \frac{L_d + L_q - (L_d - L_q)\cos(2\theta_e)}{2L_dL_q}, \tag{5.1}$$

$$\mathcal{R}'_{phb} = \frac{3}{2}\frac{1}{L_{phb}} = \frac{L_d + L_q - (L_d - L_q)\cos\left[2(\theta_e - \frac{2\pi}{3})\right]}{2L_dL_q}, \tag{5.2}$$

$$\mathcal{R}'_{phc} = \frac{3}{2}\frac{1}{L_{phc}} = \frac{L_d + L_q - (L_d - L_q)\cos\left[2(\theta_e + \frac{2\pi}{3})\right]}{2L_dL_q}, \tag{5.3}$$

to obtain a harmonic function of rotor position scaled so

$$\min \mathcal{R}'_{phN} = \mathcal{R}'_d = 1/L_d \quad \text{and} \quad \max \mathcal{R}'_{phN} = \mathcal{R}'_q = 1/L_q, \tag{5.4}$$

where $\mathcal{R}'_d$ and $\mathcal{R}'_q$ are normalized reluctances in direct and quadrature axis. This form is useful for its easy integration to SynRM mathematical model. The $\mathcal{R}'_{phN}$ can be also expressed using direct and quadrature axis reluctances as

$$\mathcal{R}'_{pha} = \mathcal{R}'_d\cos^2(\theta_e) + \mathcal{R}'_q\sin^2(\theta_e), \tag{5.5}$$

$$\mathcal{R}'_{phb} = \mathcal{R}'_d\cos^2(\theta_e + 2\pi/3) + \mathcal{R}'_q\sin^2(\theta_e - 2\pi/3), \tag{5.6}$$

$$\mathcal{R}'_{phc} = \mathcal{R}'_d\cos^2(\theta_e - 2\pi/3) + \mathcal{R}'_q\sin^2(\theta_e + 2\pi/3). \tag{5.7}$$

Looking back at Figure 5.2, the phase reluctances $\mathcal{R}'_{phN}$ can be obtained from the DC-bus current change Δi_{dc} caused by the non-zero SVM voltage vector $\boldsymbol{v}_M$ applied by the inverter for the time duration $\boldsymbol{T}_{vM}$ as

$$\mathcal{R}'_{phN} \cong \left(\frac{\Delta i_{dc}}{T_{vm}}\right) \frac{2}{3} \frac{1}{U_{dc} + R_{ph} i_N (-1)^m}, \quad \text{where } m \in M \in \langle 1; 6 \rangle \,. \tag{5.8}$$

The measurement of current change Δi_{dc} is, however, not a simple task. The SynRM usually have a large stator inductances when compared to other motor types. This is a result of a design, which favours large $L_d - L_q$ difference. At the same time, the standard PWM, as shown in Figure 2.4, generates only short periods $\boldsymbol{T}_{vM}$ during which the Δi_{dc} can be measured.

The most commonly used method of stator current measurement is the current reconstruction from voltage drops measured on bottom shunt resistors R_{sh} using operational amplifiers. This is depicted by the MC IABC block in Figure 5.1. These circuits are set-up for the measurement of complete stator current scale $\pm \max(\vec{i}_{abc})$. Using MC IABC with such configuration for Δi_{dc} measurement would very likely lead to signal with a high noise content. Existing algorithms based on Δi_{dc} measurement then usually employ additional sensor or over-sampling [RSW18, NSS20].

The proposed method is based on the Measurement Circuit of DC-bus current i_{dc} (MC IDC). It amplifies the voltage drop on the common DC-bus shunt resistor R_{shc}, as shown in Figure 5.1. Its basic principle of operation is illustrated in Figure 5.3. Compared to MC IABC, it is configured to have a much higher gain and, as a result, a smaller measurement scale $\max(i_{dc}) \ll \max(\vec{i}_{abc})$. This allows to achieve a much better resolution of the i_{dc} measurement. Such a high gain would normally lead to a quick saturation of the MC IDC output even for a small stator current amplitudes $\vec{i}_{abc}$. To avoid this, the MC IDC measurement window is being actively offset by a DAC-generated signal to be located at the predicted location of i_{dc}. The correct offset value is obtained from the $\vec{i}_{abc}$ measurements from MC IABC and knowledge of upcoming voltage vector $\boldsymbol{v}_M$, which determines the i_{dc} value as shown in Figure 5.2.

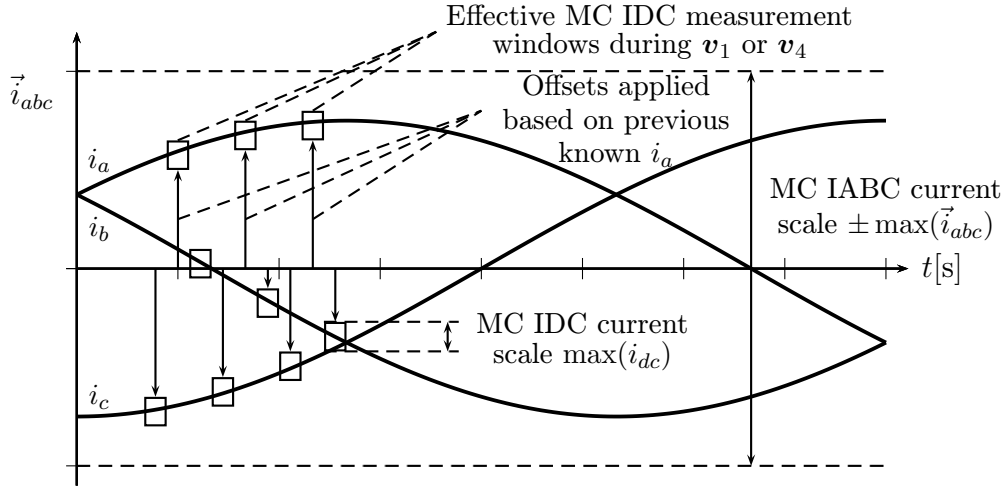

Figure 5.3: Illustration of operation of MC IDC circuit

An example of the schematic diagram of the MC IDC is shown in Figure 5.4. Its output u_{idc} leads to the ADC periphery of MCU and contains amplified information about Δi_{dc}. The u_{DD} is the operational amplifier supply voltage, which ideally limits the MC IDC output to 0 V $< u_{idc} < u_{DD}$ range. The u_{off} is a DAC-generated signal, which, offsets the measured current range to avoid output saturation and fit the predicted i_{dc} location. The circuit functions as a differential amplifier with an analog gain $\max(i_{dc})$ configured as necessary to achieve a good Δi_{dc} resolution.

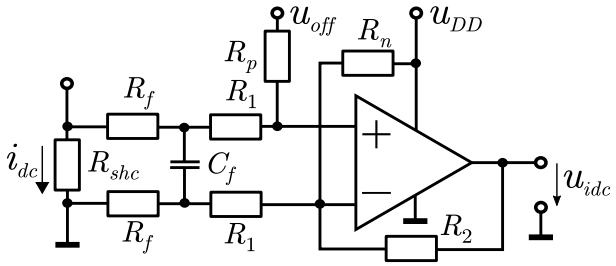

Figure 5.4: Measurement circuit of i_{dc} current MC IDC [MVB21]

Once the MC IDC is properly configured, the u_{idc} can be sampled by ADC to obtain $\Delta i_{dc} = \max(i_{dc})/u_{DD}\Delta u_{idc}$ and the u_{off} can be generated by DAC. An example of the resulting $\mathcal{R}'_{phN}$ measurement versus the rotor position θ_e obtained on a real system is shown in Figure 5.5. It can be seen that the obtained signals can be used to extract rotor position θ_e as well as machine reluctances $\mathcal{R}'_d$ and $\mathcal{R}'_q$.

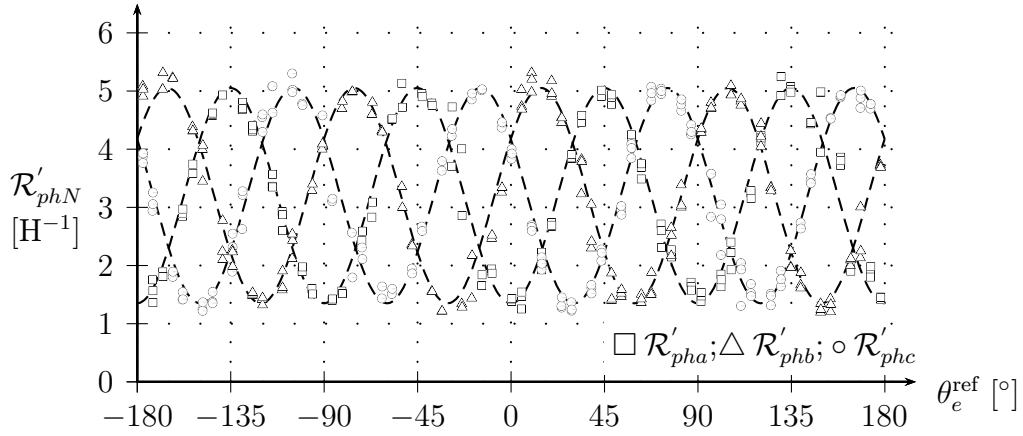

Figure 5.5: Example of $\mathcal{R}'_{phN}$ measurement obtained on a reference SynRM machine

5.2. Alignment-Swap PWM Switching Scheme

The current derivative Δi_{dc} measurement method presented in the previous section can be generally used with any such scheme, which generates non-zero voltage vectors $\boldsymbol{v}_M$. The Δi_{dc} measurement method, however, benefits from longer uninterrupted non-zero voltage vector periods $\boldsymbol{T}_{vM}$, which allow for the acquisition of higher number or more distant Δi_{dc} samples. When looking at the example of commonly used centre-aligned PWM in Figure 2.4, the periods $\boldsymbol{T}_{vM}$ are divided into halves and, what is more important, zero vectors $\boldsymbol{v}_0$ and $\boldsymbol{v}_7$ can take a significant portion of PWM period T_{PWM}. At duty cycles near to the 50 % minimum or anytime the switching edges are close to each other, this leads to short or no active

vector generation, making the Δi_{dc} measurement difficult or impossible. This led to the proposal of the alignment-swap PWM (ASPWM) switching scheme.

The principle is shown in Figure 5.6. The phase PWM signal edge alignment is swapped in every third PWM cycle to the opposite edge consequently in each phase. The non-zero voltage vectors $\boldsymbol{v}_M$ are, thus, going to align to either the beginning or the end of the PWM period once per three PWM cycles. Calculation of phase duty cycles $\vec{D}_{abc}$ remains unchanged compared to the standard SVM method described in Section 2 and the final generated fundamental voltage vector $\vec{u}_{\alpha\beta}$ will be unchanged. In case that duty cycle $\max(\vec{D}_{abc}) \rightarrow 100$ % and $\min(\vec{D}_{abc}) \rightarrow 0$ %, the voltage vectors near the PWM period edges might become too short for effective Δi_{dc} measurement. In such a case, the Δi_{dc} information can be extracted from active vectors $\boldsymbol{v}_M$ formed in the centre of the PWM period.

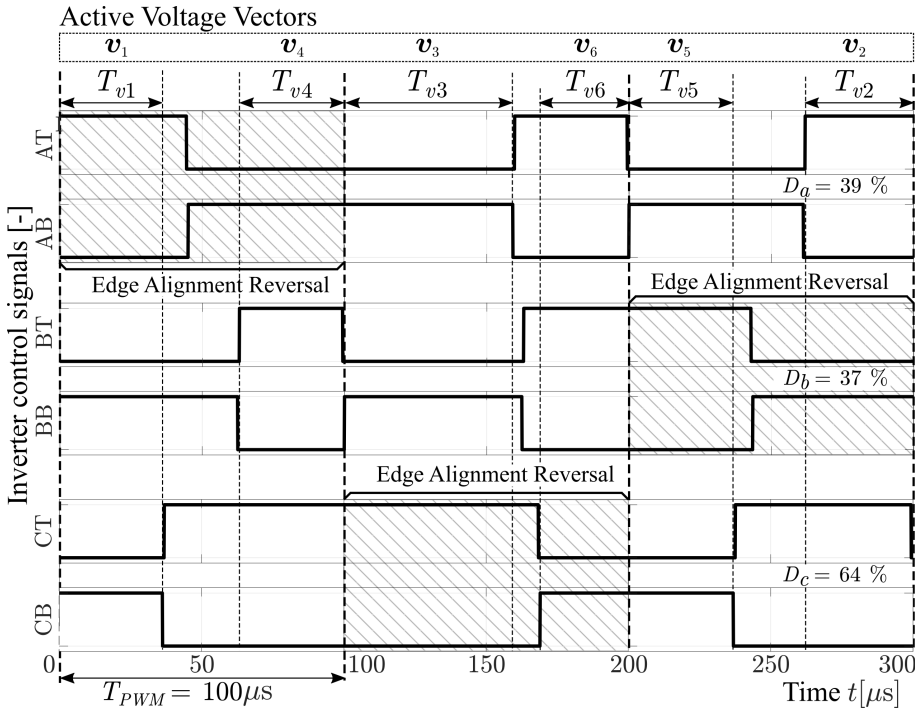

Figure 5.6: Principle of the proposed alignment-swap PWM scheme [MVB21]

An example of interaction between the ASPWM scheme and the proposed Δi_{dc} measurement method is shown in Figure 5.7. Signal u_{off} is updated by the DAC at the beginning of the PWM cycle and when the first switching event occurs, so the u_{idc} signal does not saturate during the measurement time window $\boldsymbol{T}_{vM}$ created at the PWM cycle edges. To extract the Δi_{dc} even from centre of the PWM cycle, when one of the duty cycles $\vec{D}_{abc}$ is too low or too high, a different u_{off} signal update sequence could be used.

To reconstruct $\vec{i}_{abc}$ vector as well from the phase shunt measurement, at least two bottom transistors must be conducting so the phase currents are flowing through the shunt resistors R_{sh}. The third phase current then can be calculated according to the first Kirchhoff's law $i_a + i_b + i_c = 0$ A. Such a suitable sampling locations (i.e. when dynamic events are settled) were highlighted in Figure 5.7.

The proposed ASPWM switching method effectively replaces portions of the zero vectors $\boldsymbol{v}_0$ and $\boldsymbol{v}_7$ by a pair of opposite active vectors $\boldsymbol{v}_1$ versus $\boldsymbol{v}_4$, $\boldsymbol{v}_3$ versus $\boldsymbol{v}_6$,

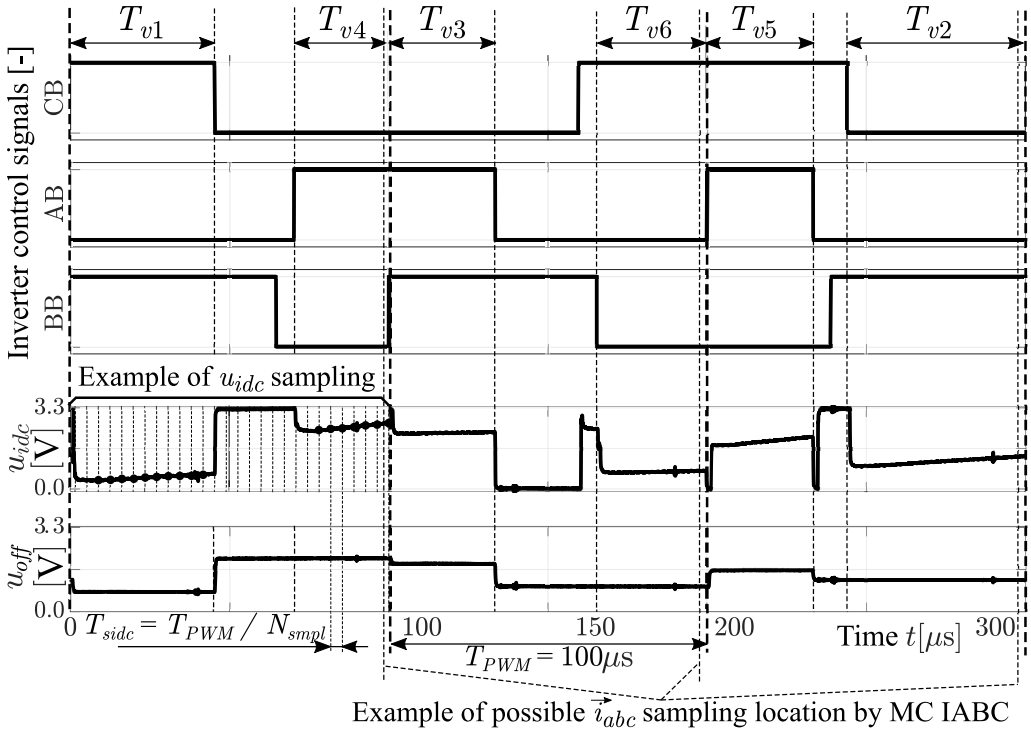

Figure 5.7: Principle of the Δi_{dc} measurement with ASPWM scheme [MVB21]

or $\boldsymbol{v}_2$ versus $\boldsymbol{v}_5$ in each PWM period. This causes an additional ripple of phase currents $\vec{i}_{abc}$. To evaluate its impact the RMS value was simulated [DW12]. The simulation was run for $U_{dc} = 400$ V and the machine stator inductance was chosen $L_{phN} = 0.3$ H, which corresponds to the worst-case scenario with the reference SynRM (see Section 1.2). The results for all voltage $\vec{u}_{\alpha\beta}$ amplitude $|\vec{u}_{\alpha\beta}|/\max(|\vec{u}_{\alpha\beta}|)$ and angle $\arg(\vec{u}_{\alpha\beta})$ are shown in Figure 5.8 and Figure 5.9. As expected, the RMS values of the ripple current component are increased for the ASPWM switching scheme so the audible noise and Total Harmonic Distortion (THD) will be worse. It can be seen that the ASPWM generates higher ripples for low $|\vec{u}_{\alpha\beta}|$ amplitude, while at the higher amplitudes its becomes comparable to CAPWM. Efficiency at higher speeds and loads will not be affected by the ASPWM method as much. Based on the maximal RMS values, the resulting power losses will be under a Watt for reference machine. This is mainly because of the relatively high inductances of SynRM machines. The ASPWM method might not be suitable for machines with smaller inductances because the current ripple power losses would increase. It is then a question, however, whether the ASPWM would even be necessary because greater Δi_{dc} changes would be more easily measurable.

When it comes to power efficiency, the ASPWM has an advantage over classic centre-aligned PWM. When comparing examples in Figure 2.4 and Figure 5.6, it can be seen that ASPWM generates only eight edges on PWM control signals per period, while the centre-aligned method produces twelve. This will reduce the semiconductor switching losses by a third, which can offset current ripple power loss.

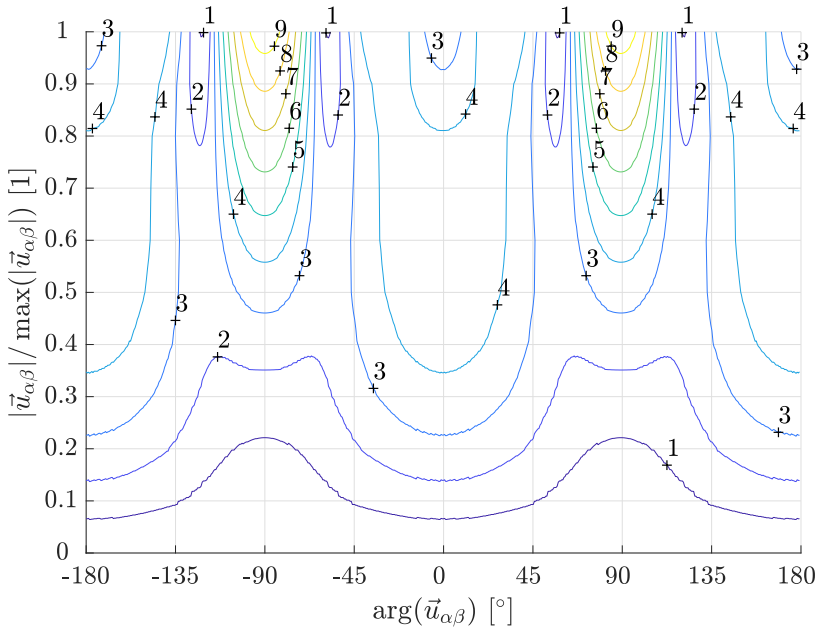

Figure 5.8: Simulated RMS value of phase current ripple in mA for CAPWM

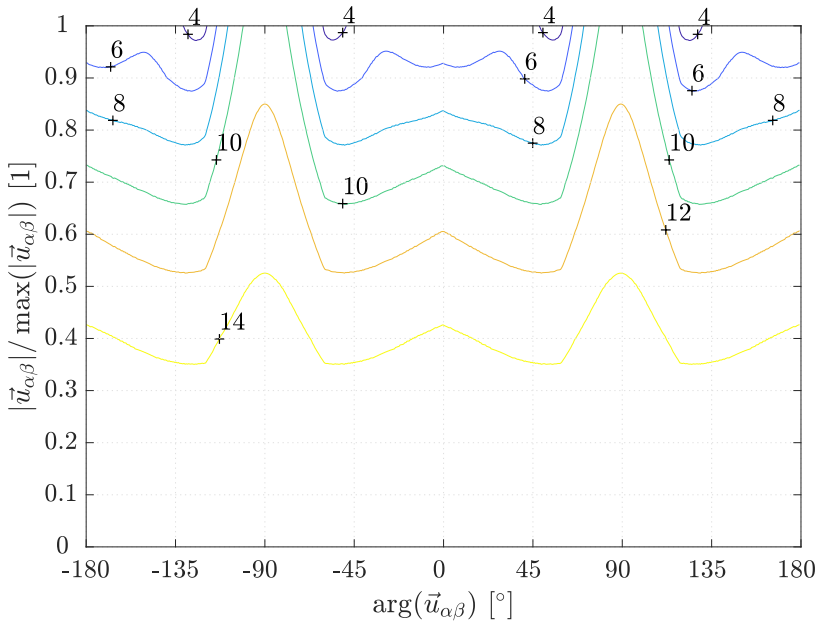

Figure 5.9: Simulated RMS value of current ripple component in mA for ASPWM

5.3. Kalman Filter

The original Kalman Filter (KF) algorithm was first proposed by R. E. Kalman in 1960 and it became very popular since then. The KF is a recursive algorithm, which minimizes the square of the estimate errors between actual system states $\vec{x}$ and the estimates $\hat{\vec{x}}$. This is done by the alternation of the prediction and correction step. The system states are updated based on the known model during the prediction step. The correction step then consists of updating the state estimates based on the measurement [WB06]. To find the true optimal solution, the noise has to have a normal distribution.

One well-known modification, the Extended Kalman Filter (EKF), is then also usable for non-linear systems under influence of Gaussian noise. As will be shown in Section 5.4, this and the ability to near-optimally merge the position and parameter information from multiple measurements made it suitable for the proposed algorithm. Disadvantages of EKF are, however, relatively high computational demands and a difficult acquisition and description of stochastic properties of measurements and estimated states [LK19, BG10].

5.3.1. Extended Kalman Filter Theory

First, we assume the discrete non-linear system state-space description

$$\begin{aligned} \vec{x}_{k+1} &= \mathbf{f}\left(\vec{x}_k, \vec{u}_k, \vec{w}_k\right), \\ \vec{y}_k &= \mathbf{h}\left(\vec{x}_k, \vec{v}_k\right), \end{aligned} \tag{5.9}$$

where $\mathbf{f}$ and $\mathbf{h}$ are non-linear time-variant system and output functions, $\vec{x}$ is the state vector, $\vec{u}$ is the vector of control variables, $\vec{y}$ is the output vector, and $\vec{w}$ and $\vec{v}$ are the process and measurement noise vectors. The noise vectors are assumed to be white noises with normal distribution $\vec{w} \sim N(0, \mathbf{Q})$ and $\vec{v} \sim N(0, \mathbf{R})$. Linearization itself is done by taking the first element of Taylor's expansion around the last state estimate $\hat{\vec{x}}$. The prediction step is than performed as

$$\begin{aligned} \hat{\vec{x}}_{k|k-1} &= \mathbf{f}\left(\hat{\vec{x}}_{k-1|k-1}, \vec{u}_k\right), \\ \mathbf{P}_{k|k-1} &= \mathbf{F}_k \mathbf{P}_{k-1|k-1} \mathbf{F}_k^{\mathrm{T}} + \tilde{\mathbf{Q}}_k, \end{aligned} \tag{5.10}$$

and the correction step as

$$\begin{aligned} \mathbf{K}_k &= \mathbf{P}_{k|k-1} \mathbf{H}_k^{\mathrm{T}} \left(\mathbf{H}_k \mathbf{P}_{k|k-1} \mathbf{H}_k^{\mathrm{T}} + \tilde{\mathbf{R}}_k\right)^{-1}, \\ \hat{\vec{x}}_{k|k} &= \hat{\vec{x}}_{k|k-1} + \mathbf{K}_k \left[\vec{y}_k - \mathbf{h}(\hat{\vec{x}}_{k|k-1}, \vec{0})\right], \\ \mathbf{P}_{k|k} &= \left(\mathbf{I} - \mathbf{K}_k \mathbf{H}_k\right) \mathbf{P}_{k|k-1}, \end{aligned} \tag{5.11}$$

where $\mathbf{P}$ is the state error covariance matrix, $\tilde{\mathbf{Q}}$ is state covariance matrix, $\tilde{\mathbf{R}}$ is measurement covariance matrix, $\mathbf{K}$ is Kalman gain, and $\mathbf{F}$ and $\mathbf{H}$ are Jacobian matrices of $\mathbf{f}$ and $\mathbf{h}$ around the state estimate. It should be noted that the linearization introduced an error into the estimate $\hat{\vec{x}}$, making the solution sub-optimal [AR15, WB06].

5.4. Proposed EKF-based Estimation Algorithm

Figure 5.1 shows the proposed EKF-based observer, which provides estimations of rotor electrical position $\hat{\theta}_e$, electrical angular speed $\hat{\omega}_e$, and stator inductances $\hat{L}_d$ and $\hat{L}_q$. All this information can be extracted from the $\mathcal{R}'_{phN}$ measurement. The following Section 5.4.1 will show a basic implementation of the EKF algorithm (further called EKF-BASIC), which can extract mentioned quantities. The stator current measurements $\vec{i}_{\alpha\beta}$ and knowledge of synchronous machine model can also be used to obtain rotor speed and position information [AR15]. Combining these two

models brings a redundancy, which can be exploited in many ways. For example, the previously published version of the proposed EKF-based estimator featured an estimation of core losses [MVB21]. The following Section 5.4.2 will show another example of the implementation of an EKF-based algorithm (called EKF-RS) that provides the stator resistance estimate $\hat{R}_s$.

5.4.1. Proposed Algorithm Variant EKF-BASIC

If we assume, that $\mathcal{R}_d^{'}$ and $\mathcal{R}_q^{'}$ are slow-changing quantities, we can form equations

$$\begin{aligned} \mathcal{R}_{pha,k}^{'} &= \mathcal{R}_{d,k}^{'}\cos^2(\theta_{e,k}) + \mathcal{R}_{q,k}^{'}\sin^2(\theta_{e,k}), \\ \mathcal{R}_{phb,k}^{'} &= \mathcal{R}_{d,k}^{'}\cos^2(\theta_{e,k}+\tfrac{2\pi}{3}) + \mathcal{R}_{q,k}^{'}\sin^2(\theta_{e,k}-\tfrac{2\pi}{3}), \\ \mathcal{R}_{phc,k}^{'} &= \mathcal{R}_{d,k}^{'}\cos^2(\theta_{e,k}-\tfrac{2\pi}{3}) + \mathcal{R}_{q,k}^{'}\sin^2(\theta_{e,k}+\tfrac{2\pi}{3}), \end{aligned} \tag{5.12}$$

$$\mathcal{R}_{d,k+1}^{'} = \mathcal{R}_{d,k}^{'}, \quad \text{and} \quad \mathcal{R}_{q,k+1}^{'} = \mathcal{R}_{q,k}^{'}. \tag{5.13}$$

Applying the Euler's discretization method to mechanical models (1.7), (1.8), and (1.9) and assuming that the ω_e does not change greatly between samples leads to

$$\omega_{e,k+1} = \omega_{e,k}, \quad \text{and} \quad \theta_{e,k+1} = \theta_{e,k} + T_s\omega_{e,k}, \tag{5.14}$$

where T_s is sampling period. Combining equations (5.13) and (5.14) leads to

$$\hat{\vec{x}} = \left[\hat{\mathcal{R}}_d^{'}, \quad \hat{\mathcal{R}}_q^{'}, \quad \hat{\omega}_e, \quad \hat{\theta}_e\right]^{\mathrm{T}} \tag{5.15}$$

and the system input vector is $\vec{u} = 0$.

As was discussed in Section 5.2, not all the $\mathrm{d}i_a/\mathrm{d}t$, $\mathrm{d}i_b/\mathrm{d}t$, and $\mathrm{d}i_c/\mathrm{d}t$ measurements are available each PWM period, depending on applied active voltage vectors $\boldsymbol{v}_M$. The proposed ASPWM scheme allows obtaining current derivative information for one of the N phases during each T_{PWM}. Hence, only one of equations (5.12) corresponding to the measured phase N will be used each step k. Available measurement (either $\mathcal{R}_{pha}^{'}$, $\mathcal{R}_{phb}^{'}$, or $\mathcal{R}_{phc}^{'}$) is going to form the measurement vector

$$\vec{y} = \mathcal{R}_{phN}^{'}. \tag{5.16}$$

The feedback non-linear time-variant system function will then be

$$\mathbf{f}\left(\hat{\vec{x}}_{k-1}, \vec{u}_k, \vec{0}\right) = \left[\hat{\mathcal{R}}_{d,k-1}^{'}, \quad \hat{\mathcal{R}}_{q,k-1}^{'}, \quad \hat{\omega}_{e,k-1}, \quad \hat{\theta}_{e,k-1} + T_s\hat{\omega}_{e,k-1}\right]^{\mathrm{T}} \tag{5.17}$$

and the non-linear output function can be assembled from (5.12) as

$$\mathbf{h}\left(\hat{\vec{x}}_k, \vec{0}\right) = \left[\hat{\mathcal{R}}_{d,k}^{'}\cos^2(\hat{\theta}_{e,k}+\theta_{phN}) + \hat{\mathcal{R}}_{q,k}^{'}\sin^2(\hat{\theta}_{e,k}+\theta_{phN})\right], \tag{5.18}$$

where θ_{phN} is stator phase offset matching the phase of actual $\mathcal{R}_{phN}^{'}$ measurement (either 0 rad, $\frac{2\pi}{3}$ rad, or $-\frac{2\pi}{3}$ rad for phases $\mathcal{R}_{pha}^{'}$, $\mathcal{R}_{phb}^{'}$, and $\mathcal{R}_{phc}^{'}$).

The Jacobian matrix of output matrix (5.18) is

$$\mathbf{H}_k = \left[\frac{\partial \mathbf{h}}{\partial \vec{x}}\right]_{\vec{x}=\hat{\vec{x}}_{k|k-1},\vec{v}=\vec{0}} = \left[\cos^2(\hat{\theta}_e + \theta_{phN}),\ \sin^2(\hat{\theta}_e + \theta_{phN}),\ 0,\ H_{16}\right], \tag{5.19}$$

where

$$H_{16} = \frac{\partial \mathcal{R}'_{phN}}{\partial \theta_e} = 2(\hat{\mathcal{R}}'_q - \hat{\mathcal{R}}'_d)\sin(\hat{\theta}_e + \theta_{phN})\cos(\hat{\theta}_e + \theta_{phN}). \tag{5.20}$$

The Jacobian matrix of discrete-time process matrix (5.17) is

$$\mathbf{F}_k = \left[\frac{\partial \mathbf{f}}{\partial \vec{x}}\right]_{\vec{x}=\hat{\vec{x}}_{k-1|k-1},\vec{u}=\vec{u}_k,\vec{w}=\vec{0}} = \begin{bmatrix} 1 & 0 & 0 & 0 \\ 0 & 1 & 0 & 0 \\ 0 & 0 & 1 & 0 \\ 0 & 0 & T_s & 1 \end{bmatrix}. \tag{5.21}$$

The covariance matrices $\tilde{\mathbf{Q}}$ and $\tilde{\mathbf{R}}$ can be adapted online using methods like the Expectation-Maximization algorithm [Moo96]. Such algorithms are, however, relatively complex. In practice, the matrices $\tilde{\mathbf{Q}}$ and $\tilde{\mathbf{R}}$ are often used as offline design parameters of EKF, which is also an approach used in this thesis.

Because there is only a single signal used as a measurement, the noise covariance matrix has a form $\tilde{\mathbf{R}} = \sigma^2_{\mathcal{R}_{ph}}$, where $\sigma_{\mathcal{R}_{ph}}$ is standard deviation of phase reluctance measurements $\mathcal{R}'_{phN}$. The value of $\sigma_{\mathcal{R}_{ph}}$ is difficult to model and in this work, it is acquired by offline analysis of recordings of real $\mathcal{R}'_{phN}$ measurements. All the states are considered to be uncorrelated, hence, the state noise covariance matrix is

$$\tilde{\mathbf{Q}} = \mathrm{diag}\left[\sigma^2_{\mathcal{R}'_d} \quad \sigma^2_{\mathcal{R}'_q} \quad \sigma^2_{\omega_e}, \quad \sigma^2_{\theta_e}\right]. \tag{5.22}$$

The states $\hat{\mathcal{R}}'_d$ and $\hat{\mathcal{R}}'_q$ can be considered to be slow-changing parameters and their standard deviations $\sigma_{\mathcal{R}'_d}$ and $\sigma_{\mathcal{R}'_q}$ can be selected close or equal to zero. The speed estimation deviation can be selected as the maximal electrical speed change with the moment of inertia J, nominal torque T_{nom} per sampling period T_s, as $\sigma_{\omega_e} = T_s T_{\mathrm{nom}}/J$. Because position θ_e is obtained as a pure integration of ω_e, its deviation will be chosen as $\sigma_{\theta_e} = 0$ rad [BSL+10, AR15].

Finally, the initialization of EKF-BASIC is done through the definition of the initial state vector $\hat{\vec{x}}_0$ and the initial covariance matrix $\mathbf{P}_0$, for example

$$\hat{\vec{x}}_0 = \left[\ 1/L_{d0},\quad 1/L_{q0},\quad 0,\quad 0\ \right], \tag{5.23}$$

where L_{d0} and L_{q0} are rough expected machine inductances. Similarly, the $\mathbf{P}_0$ can be set as a diagonal matrix, usually with sufficiently high variance values on the main diagonal, reflecting the low confidence in vector $\hat{\vec{x}}_0$.

5.4.2. Variant with Stator Resistance Measurement EKF-RS

This section will present the EKF-RS algorithm variant, which takes into account stator current $\vec{i}_{\alpha\beta}$ measurement and knowledge of the machine model to provide estimate of the stator resistance R_s as well.

First, the stator current model (1.6) with neglected core losses and dynamic inductance is assumed, as well as mechanical models (5.14). Applying Euler's discretization method leads to

$$\begin{aligned} i_{d,k} &= i_{d,k-1} + T_s \mathcal{R}'_{d,k-1} \left\{ u_{d,k} - R_s i_{d,k-1} + \omega_{e,k-1} i_{q,k-1} / \mathcal{R}'_{q,k-1} \right\}, \\ i_{q,k} &= i_{q,k-1} + T_s \mathcal{R}'_{q,k-1} \left\{ u_{q,k} - R_s i_{q,k-1} - \omega_{e,k-1} i_{d,k-1} / \mathcal{R}'_{d,k-1} \right\}, \\ \omega_{e,k} &= \omega_{e,k-1}, \quad \text{and} \quad \theta_{e,k+1} = \theta_{e,k-1} + T_s \omega_{e,k-1}. \end{aligned} \tag{5.24}$$

The above-defined models would alone be sufficient to design an EKF-based estimator, which could provide position $\hat{\theta}_e$ and speed $\hat{\omega}_e$ estimates [AR15, SKUU03]. However, to get the stator resistance $\hat{R}_s$ information, the EKF-RS will also utilize (5.12) and (5.13). This leads to state and system input vectors

$$\hat{\vec{x}} = \left[\hat{\mathcal{R}}'_d, \quad \hat{\mathcal{R}}'_q, \quad \hat{i}_d, \quad \hat{i}_q, \quad \hat{\omega}_e, \quad \hat{\theta}_e, \quad \hat{R}_s \right]^{\mathrm{T}} \quad \text{and} \quad \vec{u} = \left[u_d, \quad u_q \right]^{\mathrm{T}}. \tag{5.25}$$

The available measurements are stator currents $\vec{i}_{\alpha\beta}$ and phase reluctances $\mathcal{R}'_{pha}$, $\mathcal{R}'_{phb}$, or $\mathcal{R}'_{phc}$, which form the measurement vector

$$\vec{y} = \left[\mathcal{R}'_{phN}, \quad i_\alpha, \quad i_\beta \right]^{\mathrm{T}}. \tag{5.26}$$

The feedback non-linear time-variant system function will then be

$$\mathbf{f}\left(\hat{\vec{x}}_{k-1}, \vec{u}_k, \vec{0} \right) = \begin{bmatrix} \hat{\mathcal{R}}'_{d,k-1} \\ \hat{\mathcal{R}}'_{q,k-1} \\ \hat{i}_{d,k-1} + T_s \hat{\mathcal{R}}'_{d,k-1} \left\{ u_{d,k} - \hat{R}_{s,k-1} \hat{i}_{d,k-1} + \hat{\omega}_{e,k-1} \hat{i}_{q,k-1} / \hat{\mathcal{R}}'_{q,k-1} \right\} \\ \hat{i}_{q,k-1} + T_s \hat{\mathcal{R}}'_{q,k-1} \left\{ u_{q,k} - \hat{R}_{s,k-1} \hat{i}_{q,k-1} - \hat{\omega}_{e,k-1} \hat{i}_{d,k-1} / \hat{\mathcal{R}}'_{d,k-1} \right\} \\ \hat{\omega}_{e,k-1} \\ \hat{\theta}_{e,k-1} + T_s \hat{\omega}_{e,k-1} \\ \hat{R}_{s,k-1} \end{bmatrix}. \tag{5.27}$$

The non-linear output function can be assembled using Park's transformation matrix (1.2) for stator currents and from (5.12) as

$$\mathbf{h}\left(\hat{\vec{x}}_k, \vec{0} \right) = \begin{bmatrix} \hat{\mathcal{R}}'_{d,k} \cos^2(\hat{\theta}_{e,k} + \theta_{phN}) + \hat{\mathcal{R}}'_{q,k} \sin^2(\hat{\theta}_{e,k} + \theta_{phN}) \\ \cos(\hat{\theta}_{e,k}) i_{d,k} \quad - \sin(\hat{\theta}_{e,k}) i_{q,k} \\ \sin(\hat{\theta}_{e,k}) i_{d,k} \quad + \cos(\hat{\theta}_{e,k}) i_{q,k} \end{bmatrix}. \tag{5.28}$$

The Jacobian matrix of output matrix (5.28) is

$$\mathbf{H}_k = \left[\frac{\partial \mathbf{h}}{\partial \vec{x}}\right]_{\vec{x}=\hat{\vec{x}}_{k|k-1},\vec{v}=\vec{0}} = \tag{5.29}$$

$$= \begin{bmatrix} \cos^2(\hat{\theta}_{e,k}+\theta_{phN}) & \sin^2(\hat{\theta}_{e,k}+\theta_{phN}) & 0 & 0 & 0 & H_{16} & 0 \\ 0 & 0 & \cos(\hat{\theta}_{e,k}) & -\sin(\hat{\theta}_{e,k}) & 0 & H_{26} & 0 \\ 0 & 0 & \sin(\hat{\theta}_{e,k}) & \cos(\hat{\theta}_{e,k}) & 0 & H_{36} & 0 \end{bmatrix}, \tag{5.30}$$

where H_{16} is defined in (5.20) and

$$H_{26} = -\sin(\hat{\theta}_{e,k})\hat{i}_{d,k} - \cos(\hat{\theta}_{e,k})\hat{i}_{q,k} \quad \text{and} \quad H_{36} = \cos(\hat{\theta}_{e,k})\hat{i}_{d,k} - \sin(\hat{\theta}_{e,k})\hat{i}_{q,k}. \tag{5.31}$$

The Jacobian matrix of process matrix (5.27) is

$$\mathbf{F}_k = \left[\frac{\partial \mathbf{f}}{\partial \vec{x}}\right]_{\vec{x}=\hat{\vec{x}}_{k-1|k-1},\vec{u}=\vec{u}_k,\vec{w}=\vec{0}} = \begin{bmatrix} 1 & 0 & 0 & 0 & 0 & 0 & 0 \\ 0 & 1 & 0 & 0 & 0 & 0 & 0 \\ F_{31} & F_{32} & F_{33} & F_{34} & F_{35} & F_{36} & F_{37} \\ F_{41} & F_{42} & F_{43} & F_{44} & F_{45} & F_{46} & F_{47} \\ 0 & 0 & 0 & 0 & 1 & 0 & 0 \\ 0 & 0 & 0 & 0 & T_s & 1 & 0 \\ 0 & 0 & 0 & 0 & 0 & 0 & 1 \end{bmatrix}, \tag{5.32}$$

where

$$\begin{aligned} F_{31} &= \tfrac{\partial i_d}{\partial \mathcal{R}'_d} = T_s\left\{u_{d,k} - \hat{R}_{s,k-1}\hat{i}_{d,k-1} + \hat{\omega}_{e,k-1}\hat{i}_{q,k-1}/\hat{\mathcal{R}}'_{q,k-1}\right\}, \\ F_{32} &= \tfrac{\partial i_d}{\partial \mathcal{R}'_q} = -T_s\hat{\mathcal{R}}'_{d,k-1}\hat{\omega}_{e,k-1}\hat{i}_{q,k-1}/\hat{\mathcal{R}}'^2_{q,k-1}, \\ F_{33} &= \tfrac{\partial i_d}{\partial i_d} = 1 - T_s\hat{R}_{s,k-1}\hat{\mathcal{R}}'_{d,k-1}, \quad F_{34} = \tfrac{\partial i_d}{\partial i_q} = T_s\hat{\omega}_{e,k-1}\hat{\mathcal{R}}'_{d,k-1}/\hat{\mathcal{R}}'_{q,k-1}, \\ F_{35} &= \tfrac{\partial i_d}{\partial \omega_e} = T_s\hat{i}_{q,k-1}\hat{\mathcal{R}}'_{d,k-1}/\hat{\mathcal{R}}'_{q,k-1}, \quad F_{36} = \tfrac{\partial i_d}{\partial \theta_e} = T_s\hat{\mathcal{R}}'_{d,k-1}u_{q,k}, \\ F_{37} &= \tfrac{\partial i_d}{\partial R_s} = -T_s\hat{\mathcal{R}}'_{d,k-1}\hat{i}_{d,k-1}, \end{aligned} \tag{5.33}$$

$$\begin{aligned} F_{41} &= \tfrac{\partial i_q}{\partial \mathcal{R}'_d} = T_s\hat{\mathcal{R}}'_{q,k-1}\hat{\omega}_{e,k-1}\hat{i}_{d,k-1}/\hat{\mathcal{R}}'^2_{d,k-1}, \\ F_{42} &= \tfrac{\partial i_q}{\partial \mathcal{R}'_q} = T_s\left\{u_{q,k} - \hat{R}_{s,k-1}\hat{i}_{q,k-1} - \hat{\omega}_{e,k-1}\hat{i}_{d,k-1}/\hat{\mathcal{R}}'_{q,k-1}\right\}, \\ F_{43} &= \tfrac{\partial i_q}{\partial i_d} = -T_s\hat{\omega}_{e,k-1}\hat{\mathcal{R}}'_{q,k-1}/\hat{\mathcal{R}}'_{d,k-1}, \quad F_{44} = \tfrac{\partial i_q}{\partial i_q} = 1 - T_s\hat{R}_{s,k-1}\hat{\mathcal{R}}'_{q,k-1}, \\ F_{45} &= \tfrac{\partial i_q}{\partial \omega_e} = -T_s\hat{i}_{d,k-1}\hat{\mathcal{R}}'_{q,k-1}/\hat{\mathcal{R}}'_{d,k-1}, \quad F_{46} = \tfrac{\partial i_q}{\partial \theta_e} = -T_s\hat{\mathcal{R}}'_{q,k-1}u_{d,k}, \\ F_{47} &= \tfrac{\partial i_q}{\partial R_s} = -T_s\hat{\mathcal{R}}'_{q,k-1}\hat{i}_{q,k-1}. \end{aligned} \tag{5.34}$$

Note that F_{36} and F_{46} were obtained by integrating the Park's transformation matrix $\mathbf{T}_{dq}^{\alpha\beta}(\theta_e)$ from (1.2) into process Jacobian matrix $\mathbf{F}$.

Just like in the case of the EKF-BASIC algorithm, the stochastic properties of the state estimate and measurements will be modelled via manually-set constant covariance matrices $\tilde{\mathbf{Q}}$ and $\tilde{\mathbf{R}}$. Measurements (5.26) are considered to be uncorrelated, therefore the measurement noise covariance matrix has the form

$$\tilde{\mathbf{R}} = \operatorname{diag}\left[\sigma^2_{\mathcal{R}_{ph}}, \quad \tfrac{2}{3}\sigma_i^2, \quad \tfrac{2}{3}\sigma_i^2\right], \tag{5.35}$$

where $\sigma_{\mathcal{R}_{ph}}$ and σ_i are standard deviations of phase reluctance $\mathcal{R}'_{phN}$ and $\vec{i}_{\alpha\beta}$ current measurements. The value of $\sigma_{\mathcal{R}_{ph}}$ is assumed to be selected just like for the EKF-

BASIC algorithm. Variance σ_i^2 can be modelled as the ADC discretization error and the noise introduced by measurement circuit MC IABC, which leads to

$$\sigma_i^2 = \left(\frac{\max(\vec{i}_{abc})}{\sqrt{12} \cdot 2^{N_{ADC}}} \right)^2 + \mathrm{EIN}^2 \left(\frac{\max(\vec{i}_{abc})}{u_{DD}} + \frac{1}{R_{sh}} \right)^2, \tag{5.36}$$

where $\max(\vec{i}_{abc})$ is the phase current measurement scale, N_{ADC} is the number of ADC bits, R_{sh} is the shunt resistance, u_{DD} is the maximal voltage measurable by ADC, and EIN is the equivalent input noise of the operational amplifier [BSL+10, AR15, CM18]. The resulting current variance in the two-phase stator $\alpha\beta$ reference frame can be calculated by taking into account Clarke's transformation as

$$\mathrm{var}\{i_\alpha\} = \mathrm{var}\left\{ \frac{2}{3} i_a - \frac{1}{3} i_b - \frac{1}{3} i_c \right\} = \frac{4}{9}\sigma_i^2 + \frac{1}{9}\sigma_i^2 + \frac{1}{9}\sigma_i^2 = \frac{2}{3}\sigma_i^2, \tag{5.37}$$

$$\mathrm{var}\{i_\beta\} = \mathrm{var}\left\{ \frac{1}{\sqrt{3}} i_b - \frac{1}{\sqrt{3}} i_c \right\} = \frac{1}{3}\sigma_i^2 + \frac{1}{3}\sigma_i^2 = \frac{2}{3}\sigma_i^2. \tag{5.38}$$

The states will also be considered to be uncorrelated, hence, the state noise covariance matrix is also diagonal, and has the form

$$\tilde{\mathbf{Q}} = \mathrm{diag}\left[\sigma_{\mathcal{R}'_d}^2, \quad \sigma_{\mathcal{R}'_d}^2, \quad \tfrac{2}{3}\sigma_i^2, \quad \tfrac{2}{3}\sigma_i^2, \quad \sigma_{\omega_e}^2, \quad \sigma_{\theta_e}^2, \quad \sigma_{R_s}^2 \right]. \tag{5.39}$$

Setup of $\sigma_{\mathcal{R}'_d}$, $\sigma_{\mathcal{R}'_q}$, σ_{ω_e}, and σ_{θ_e} was already discussed in Section 5.4.1. The stator resistance estimate deviation σ_{R_s} should be chosen as a small or zero value because the stator resistance estimate will be a slow-changing quantity. The variance of the stator currents in the rotating dq reference frame can be estimated by taking into account the Park's transformation as

$$\mathrm{var}\{i_d\} = \mathrm{var}\{i_\alpha \cos(\hat{\theta}_e) + i_\beta \sin(\hat{\theta}_e)\} \simeq \cos^2(\hat{\theta}_e)\frac{2}{3}\sigma_i^2 + \sin^2(\hat{\theta}_e)\frac{2}{3}\sigma_i^2 = \frac{2}{3}\sigma_i^2, \tag{5.40}$$

$$\mathrm{var}\{i_q\} = \mathrm{var}\{-i_\alpha \sin(\hat{\theta}_e) + i_\beta \cos(\hat{\theta}_e)\} \simeq \sin^2(\hat{\theta}_e)\frac{2}{3}\sigma_i^2 + \cos^2(\hat{\theta}_e)\frac{2}{3}\sigma_i^2 = \frac{2}{3}\sigma_i^2. \tag{5.41}$$

Note that the above expression was simplified by considering zero rotor position variance σ_{θ_e} and should be treated as a rough setup.

The initialization of EKF-RS will be analogous to the EKF-BASIC variant as well. The initial state vector $\hat{\vec{x}}_0$ can be set as

$$\hat{\vec{x}}_0 = \left[\; 1/L_{d0}, \quad 1/L_{q0}, \quad 0, \quad 0, \quad 0, \quad 0, \quad R_{s0} \; \right], \tag{5.42}$$

where L_{d0}, L_{q0}, and R_{s0} are rough expected machine parameters. Similarly, the $\mathbf{P}_0$ can be set as a diagonal matrix, usually with sufficiently high variance values for currents $\hat{\vec{i}}_{dq}$, speed $\hat{\omega}_e$, and position $\hat{\theta}_e$ because of low confidence in initial state.

6. Experimental Analysis

The goal of this chapter is to compare the performance of the SynRM control algorithms proposed in Section 5 on a real system with other, commonly used, state-of-the-art sensorless algorithms listed in Section 2, as well as the sensor-based control.

6.1. The Measurement Setup

All measurements were done on reference 550 W machine from KSB manufacturer, which parameters were already presented in Section 1.2. This SynRM machine was integrated into testbench, which high-level block diagram is in Figure 6.1 and photography of its setup is in Figure 6.2. The shaft of the SynRM motor was connected to the 3.5 kW PMSM motor Allan Bradley F-4030-Q-H00AX to act as a loading generator. A benefit of this machine is the integrated 12-bit encoder, which, thanks to the co-axial motor-to-load setup, was used to get reference rotor position θ_e of both the SynRM motor and the load PMSM generator. Both the motor and generator inverter shared the same DC-bus rail so the generated power was used to immediately cover a part of the input power of the SynRM motor.

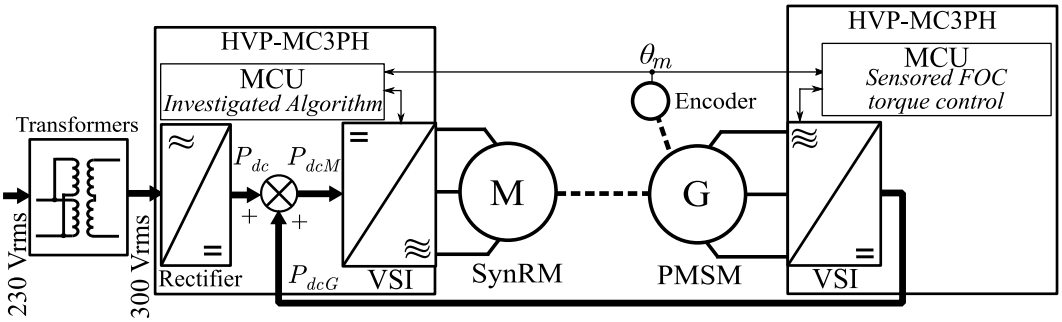

Figure 6.1: High-level block diagram of the experimental set-up

The FOC algorithm on the SynRM side of this block diagram might differ based on which exact algorithm was investigated. See Section 6.2 for more details. Both the motor and the load were driven using NXP HVP-MC3PH high-voltage inverters, which are able to provide roughly up to one kW of three-phase AC power. The motor-side inverter was modified to feature the MC IDC circuit, which, as described in Section 5.1, was used to acquire necessary i_{dc} current derivative measurements to support the proposed algorithms. It was configured to measure DC-bus current in range $i_{dc} \in \langle -3.05; 3.75 \rangle$ A, with gain $K_R R_p R_{shc} = 4.21$ V/A. The MC IABC circuit was set to measure $i_{abc} \in \langle -8; 8 \rangle$ A and the MC UDC measurement scale to $\max(U_{dc}) = 433$ V. For comparison, if the MC IABC circuit was used to measure Δi_{dc}, it would offer a 20-times lower resolution. The PWM frequency, phase current sampling frequency, and the current control loop frequency were set identically to 10 kHz. Note that maximal SynRM speed achievable under full load was 900 rpm due to inverter DC-bus voltage limitation. This should not impact validity of conclusions drawn from experiments though.

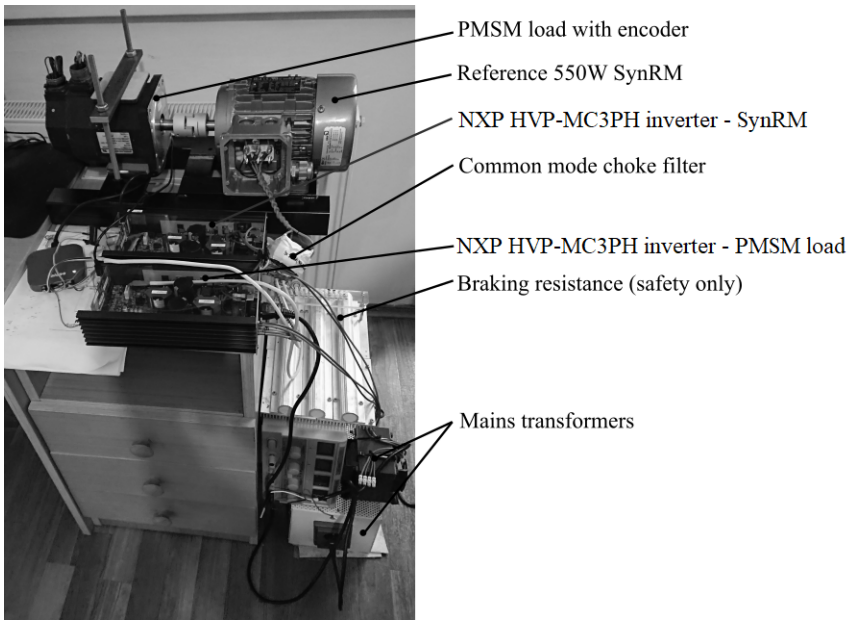

Figure 6.2: Photography of the experimental testbench setup

6.2. Implementation of Investigated Estimators

To allow a relative comparison of performance the proposed EKF-based algorithms EKF-BASIC and EKF-RS, other position and speed sources with various properties were implemented as well:

- *Encoder measurement* - A conventionally true position and speed was obtained using 12-bit encoder sensor. Both the ASPWM and the centre-aligned PWM switching schemes were implemented to allow investigation of impact of using ASPWM scheme.

- *High-frequency injection algorithm* - The saliency-based algorithm with harmonic voltage vector injection into d-axis was used as a reference for low-speed.

- *EEMF observer* - The EEMF-based algorithm was used as a reference at medium and high speeds. The basic EEMF algorithm is not naturally adaptive, hence, several different variations were implemented:

  - *EEMF observer with constant model parameters* - A basic algorithm version with constant $\hat{R}_s$ and $\hat{L}_q$ values. Considered in order to evaluate the impact of using non-adaptive algorithm. This is a valuable reference as this approach is often chosen in practical applications [HKS99, KSG+14].
  - *EEMF observer with LUT* - The algorithm version with constant $\hat{R}_s$ value and inductances $\hat{L}_d'$ and $\hat{L}_q$ provided by the LUT table. This modification was included to evaluate what performance can be achieved with accurate parameters obtained offline. The algorithm might not be considered to be truly adaptive as the LUT does not reflect the change of inductances (e.g. due to temperature change).
  - *EEMF observer with RLS* - The algorithm version with $\hat{R}_s$, $\hat{L}_d'$, and $\hat{L}_q$ parameters provided online by Recursive Least Square algorithm.

6.3. Measurement Results

This section presents the results of conducted experiments. Section 6.3.1 will focus on the general position and speed estimation capability of EKF-BASIC and EKF-RS. The main analysis, which response to estimation accuracy goals formulated in Section 4.3, is then available in Section 6.3.2. Finally, Section 6.3.3 will analyze the impact on power losses by the ASPWM scheme used by EKF-BASIC and EKF-RS and the impact of signal injections required by HFI and RLS.

6.3.1. Basic Speed and Position Tracking

The basic capability of EKF-BASIC and EKF-RS estimators of position and speed tracking in the full speed range is shown in Figure 6.3 and Figure 6.4. The position error θ_e^{err} spiked up to 25 degrees but dropped during stead-state. Deeper accuracy analysis is available in Section 6.3.2.

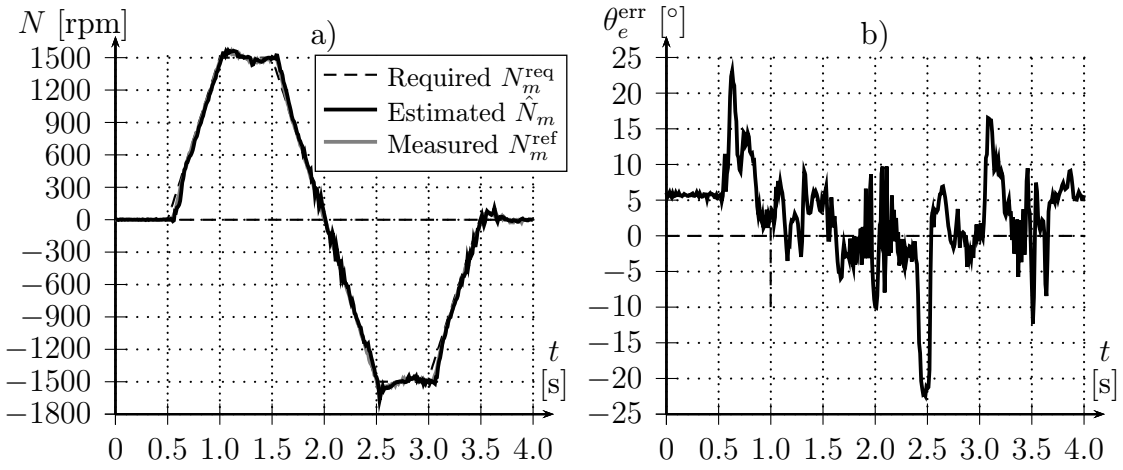

Figure 6.3: EKF-BASIC a) speed estimate and b) position error in full speed range

It is noticeable, that the overall speed and position tracking ability of EKF-BASIC and EKF-RS are very similar. This was expected because the additional machine model in the EKF-RS mainly serves to estimate the stator resistance $\hat{R}_s$.

The speed reversal during the experiment also shows the ability of both algorithms to run at low-speed or even standstill, which is a considerable benefit when compared to EEMF algorithm.

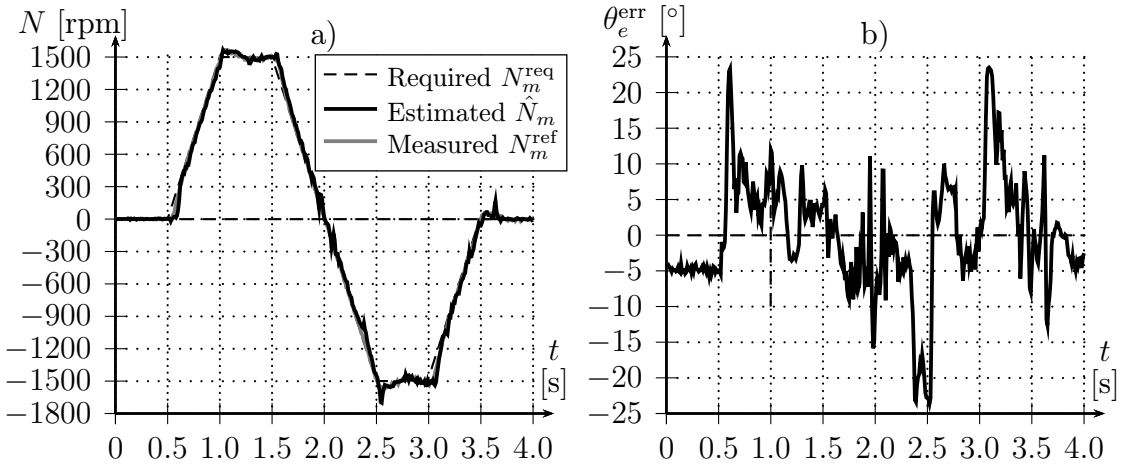

Figure 6.4: EKF-RS a) speed estimate and b) position error in full speed range

6.3.2. Steady-State Parameter Estimation Accuracy

The data for steady-state estimation accuracy were measured at points:

- Speed N_m was set from 100 rpm to 900 rpm with 200 rpm step. The EEMF-based algorithms were tested at $|N_m^{\text{req}}| \geq 500$ rpm and HFI at lower speed. The EKF-BASIC and EKF-RS algorithms were verified at full speed range.
- Load T_l was set from 0.5 Nm to 3.5 Nm with 0.5 Nm step.
- Current angle $\hat{\theta}_I$ was set from 40 degrees to 76 degrees with two-degree steps.

Position Estimation Accuracy

Results for all considered combinations of algorithms are available in histograms in Figure 6.5. Bin size for all histograms was selected to half of degree. The EEMF with constant parameter setting shows by far the greatest θ_e^{err} error, despite being a popular option in the literature. The RLS implementation achieved low θ_e^{err} error values, but with an increased dependency on the current angle $\hat{\theta}_I$ value (i.e. large variation). The best performance can be achieved with accurately identified parameters provided by LUT tables. Although it should be noted, that any discrepancy between such offline-obtained parameters and the actual machine parameters led to significant position error θ_e^{err}. The $\hat{L}_d$ inductance errors $\delta_{L_d} = \pm 25$ % caused position errors close to ten degrees, which is more than was predicted by simulation in Figure 4.3. Overall, the results show that EKF-BASIC and EKF-RS algorithms do not offer better position estimation accuracy, then correctly configured state-of-the-art algorithms. At the same time, however, the proposed algorithms provided acceptable and consistent performance in full measured load and speed range, while not being reliant on precise knowledge of machine parameters.

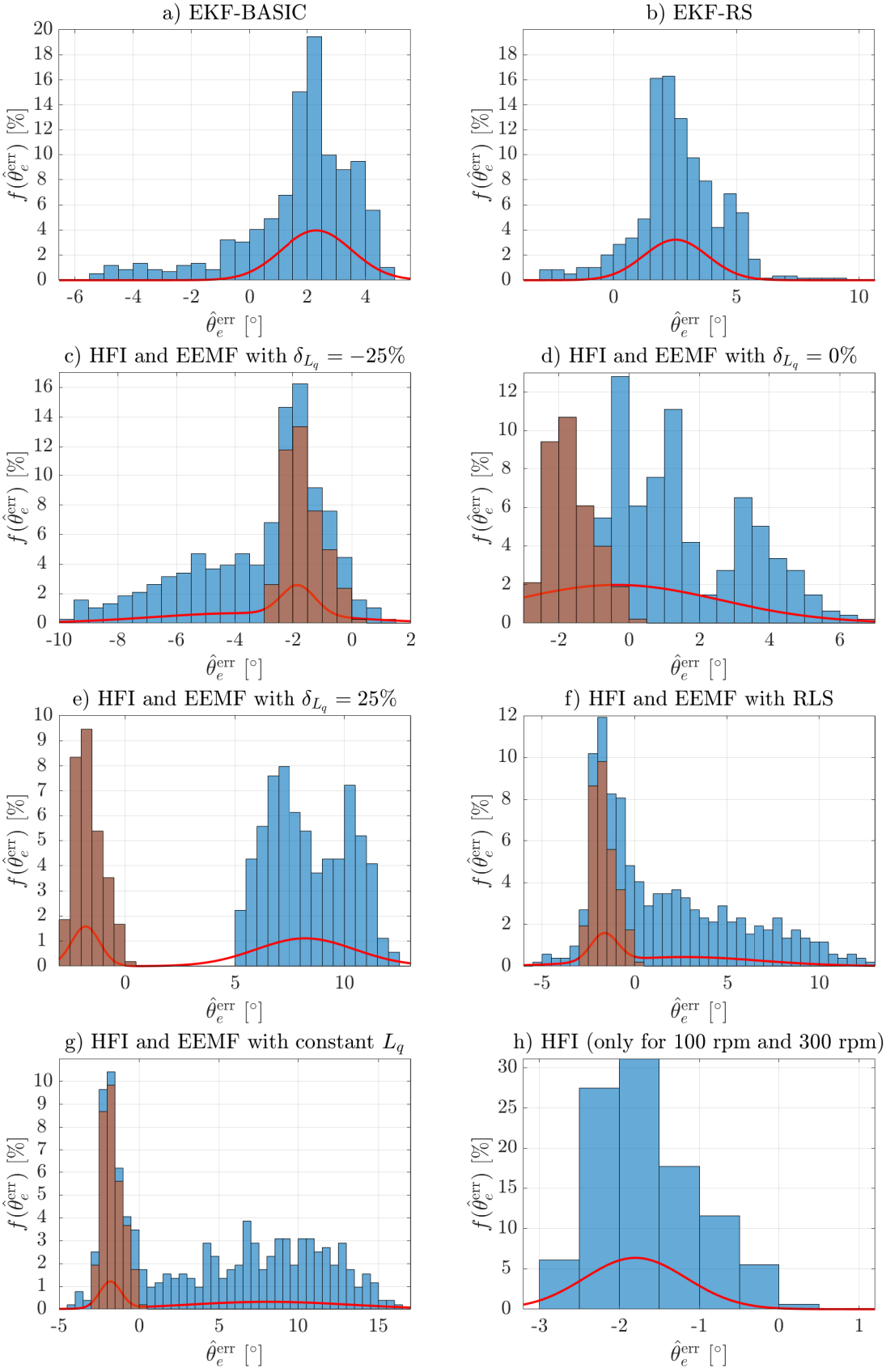

Figure 6.5: Histograms of measured $\hat{\theta}_e^{\text{err}}$ for a) EKF-BASIC, b) EKF-RS, h) HFI only, and HFI with c-e) EEMF+LUT, f) EEMF+RLS, and g) constant EEMF

Inductance and Resistance Estimation Accuracy

This section compares inductance and resistance estimation accuracy of EKF-BASIC, EKF-RS, and RLS algorithms. The relative errors of resistance δ_{R_s}, direct axis inductance δ_{L_d}, and quadrature axis inductance δ_{L_q} estimates were obtained in relation to offline-measured values stated in Section 1.2. Histograms in Figure 6.6 and Figure 6.7 show a comparison over all the measured operation points. Histograms used $\delta_{L_d} = \delta_{L_q} = 5$ % or $\delta_{R_s} = 20$ % bins.

Both proposed algorithms showed errors, which generally met the goals set in Section 4.3, while the RLS algorithm showed lower performance. Although the original publication with the implemented RLS algorithm showed similar errors, the measurement results should not be interpreted as if better performance could not be reached [ITDO06]. It can, however, be claimed that highly accurate online parameter adaptation is not a trivial task. The EKF-BASIC and EKF-RS estimate errors (namely for the $\hat{R}_s$) were likely caused by deformations in $\mathcal{R}'_{phN}$ measurements, which highlight a need for good hardware setup and postprocessing of samples.

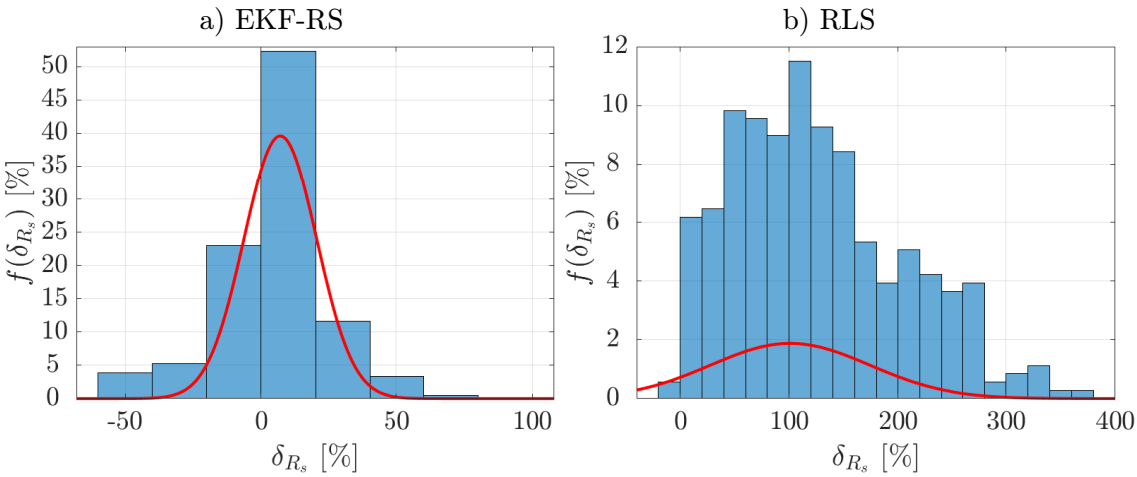

Figure 6.6: Stator resistance $\hat{R}_s$ estimates and corresponding histograms of estimate error δ_{R_s} for a) EKF-RS and b) RLS algorithms

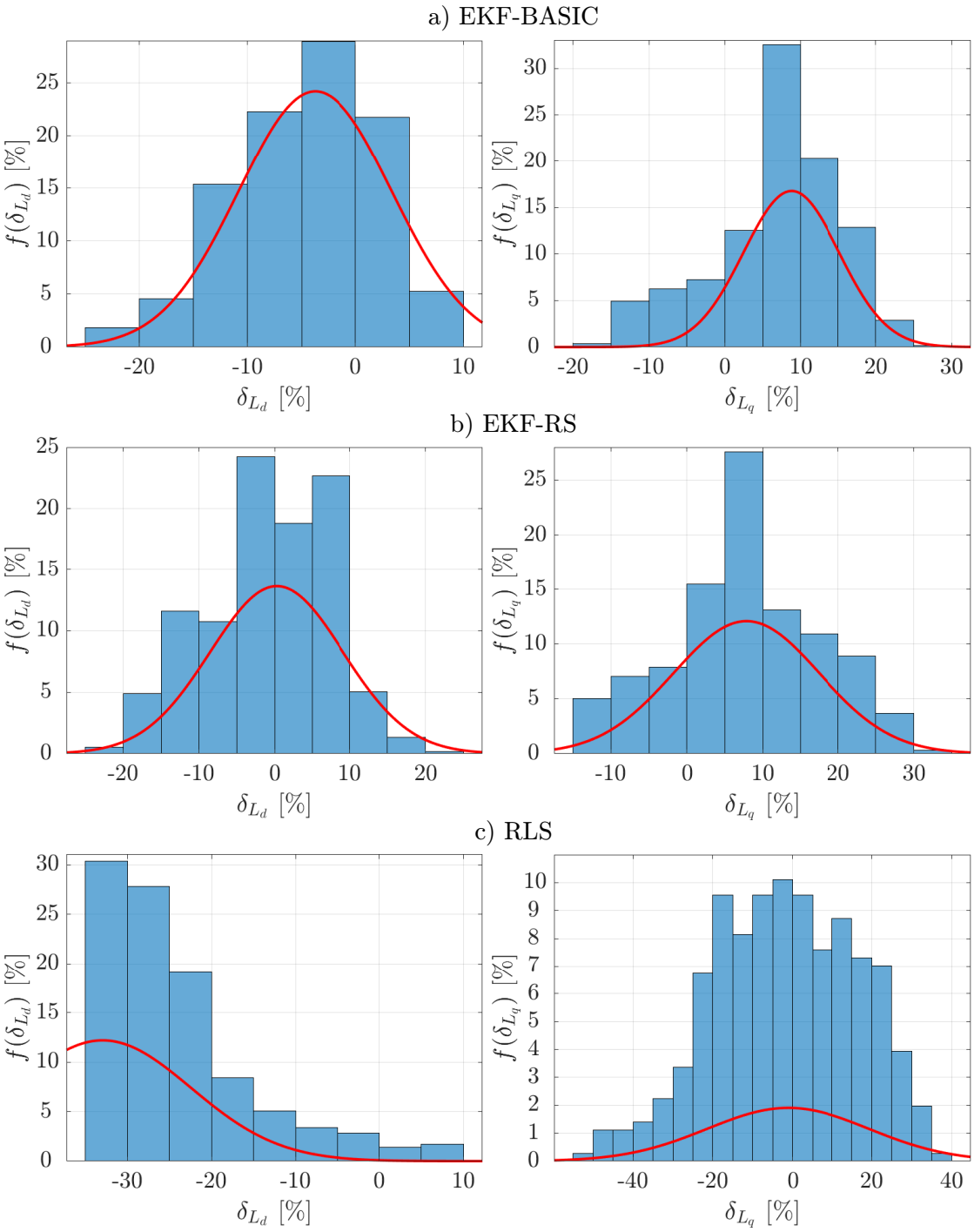

Figure 6.7: Inductances $\hat{L}_d$ and $\hat{L}_q$ and corresponding histograms of estimate errors δ_{L_d} and δ_{L_q} for a) EKF-BASIC, b) EKF-RS, and c) RLS algorithms

6.3.3. Comparison of Optimal Power Trajectories

This section will analyze the same data as in Section 6.3.2 in order to determine the impact of signal injections used by HFI and RLS algorithms and the ASPWM switching scheme to optimal MTPA and ME trajectory. The CAPWM switching

scheme with no injection will be considered as a reference. Note that the optimal current angle θ_I was maintained by the encoder sensor.

To evaluate the impact of using ASPWM switching scheme or injections, like the PRBS signal injection used by RLS algorithm and the harmonic signal injection used by HFI, Figure 6.8 shows the stator currents I_m and the inverter input powers P_{dcM} corresponding to the optimal MTPA and ME trajectories in comparison to centre-aligned PWM scheme with no injections (a reference configuration). As expected, the additional PRBS and harmonic injections caused a measurable increase of both the stator current amplitude ΔI_m and input power ΔP_{dcM}. Results in Figure 6.8d show an increase of input power ΔP_{dcM} in units of Watts for both the PRBS and the harmonic injection. The exact increase in a real application would, of course, be a matter of parameters of the injected signal, but it is safe to assume that any injection will always lead to additional power losses. As for the alignment-swap PWM switching scheme, used by the EKF-BASIC and the EKF-RS algorithms, it was discussed in Section 5.2 that the method leads to elevated current ripple, but also reduces the switching power losses by factor of one third. Experimental results in Figure 6.8f show a reduction in input power ΔP_{dcM} by units of Watts, which generally confirms this prediction and shows the potential value of the method. This is true especially for drives with high stator inductances, where the increase in THD and audible noise is not as significant.

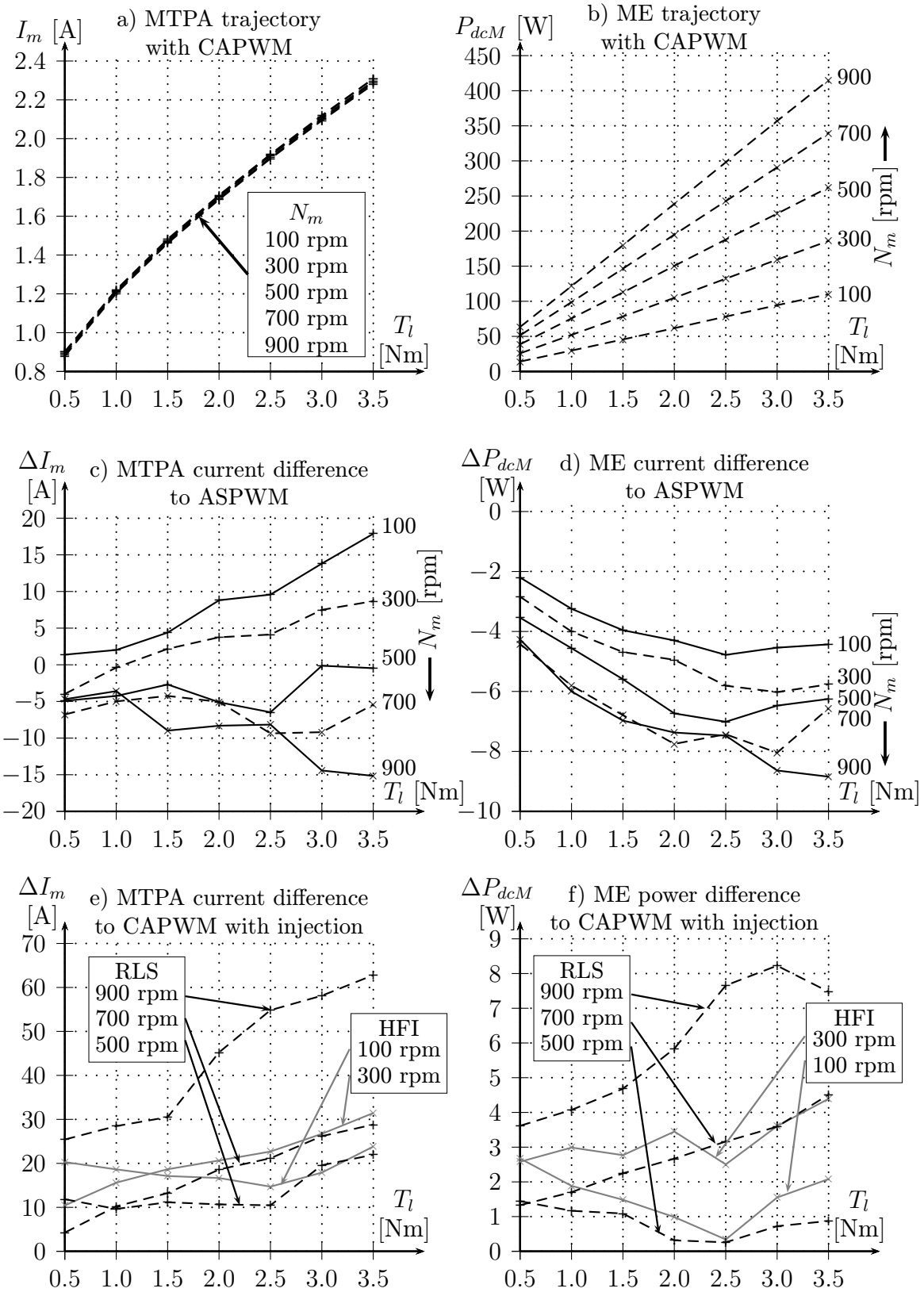

Figure 6.8: Optimal a) MTPA and b) ME trajectories with CAPWM and relative current ΔI_m and input power ΔP_{dcM} differences when using c-d) ASPWM scheme or e-f) signal injections

Conclusions

This thesis focused on the development of SynRM state and parameter estimation algorithm suitable for sensorless power-optimal applications. Chapter 1 of this thesis showed the SynRM machine mathematical model and its significant inductance non-linearity caused by magnetic saturation. Chapter 2 and Chapter 3 then presented the existing SynRM sensorless state and parameter estimation, as well as, power-optimization algorithms. Evaluation of the SynRM power-optimal sensorless control state-of-the-art was conducted in Chapter 4. The analysis resulted in goals listed in Section 4.3, which were pursued by the algorithms proposed in this thesis. In summary, it was deemed that sensorless position, speed, and inductance estimator is necessary, capable of operating in full-speed range with a good estimation accuracy but without costly hardware and need of significant signal injection.

The proposed method featured three novel ideas:

- The current derivative measurement method is described in Section 5.1. The simple and low-cost measurement circuit MC IDC allows measuring Δi_{dc} with improved accuracy. As shown by the proposed EKF-BASIC algorithm, this measurement is enough to obtain phase reluctances, rotor position, and speed.

- The alignment-swap PWM switching scheme shown in Section 5.2 allows to measure the current derivatives even for small duty cycle. Method introduced increased stator current ripple but also reduced inverter switching losses.

- Additional measurements and machine models were used as redundancy via the extended Kalman filter. For example, the proposed EKF-RS algorithm estimated the resistance $\hat{R}_s$ and the previously published method provided core loss estimate [MVB21]. Other similar modifications can be derived.

The use of the ASPWM scheme and the phase reluctance measurement method based on the MC IDC circuit allowed to meet the requirement of low additional cost and ability to operate at low-speed and standstill. The position and inductance estimate accuracy goals were verified and compared in Chapter 6. Carefully tuned existing methods (e.g. EEMF with inductances from LUT), can generally achieve a great position estimation performance, however, it quickly deteriorates when LUT parameters do not match. In contrast, the proposed method is highly adaptive and can deliver a robust performance with previously unknown or changing inductances.

Overall the presented adaptive sensorless state and parameter estimation method met the goals defined for this thesis. Its parts or as a whole, it might serve as an interesting alternative for SynRM-based high power-efficient applications.

Relevant Author's Bibliography

[MVB21] Z. Mynar, P. Vaclavek, and P. Blaha. Synchronous Reluctance Motor Parameter and State Estimation Using Extended Kalman Filter and Current Derivative Measurement. *IEEE Transactions on Industrial Electronics*, 68(3):1972–1981, Mar. 2021. DOI: 10.1109/TIE.2020.2973897.

[MVV16] Z. Mynar, L. Vesely, and P. Vaclavek. PMSM Model Predictive Control With Field-Weakening Implementation. *IEEE Transactions on Industrial Electronics*, 63(8):5156–5166, Apr. 2016. DOI: 10.1109/TIE.2016.2558165.

[Myn15] Z. Mynar. Linear Model Predictive Control of Induction Machine. *Proceedings of the 21th Conference STUDENT EEICT 2015*, pages 465–469, Apr. 2015. ISBN: 978-80-214-5148-3.

[Myn16] Z. Mynar. Power Optimized Control of Synchronous Reluctance machine. *Proceedings of the 22th Conference STUDENT EEICT 2016*, pages 441–445, Apr. 2016. ISBN: 978-80-214-5350-0.

[VM17] L. Vesely and Z. Mynar. Model predictive control of SPMSM based on FPGA and processor. In *2017 IEEE International Conference on Industrial Technology (ICIT)*, pages 324–329, Mar. 2017. DOI: 10.1109/ICIT.2017.7913104.

Bibliography

[AR15] J. Antons and T. Rösmann. Self-sensing control of a synchronous reluctance machine using an extended Kalman filter. In *2015 IEEE International Conference on Industrial Technology (ICIT)*, pages 831–839, Mar. 2015. DOI: 10.1109/ICIT.2015.7125201.

[BCP16] N. Bedetti, S. Calligaro, and R. Petrella. Stand-Still Self-Identification of Flux Characteristics for Synchronous Reluctance Machines Using Novel Saturation Approximating Function and Multiple Linear Regression. *IEEE Transactions on Industry Applications*, 52(4):3083–3092, Jul. 2016. DOI: 10.1109/TIA.2016.2535413.

[BG10] O. Benjak and D. Gerling. Review of position estimation methods for IPMSM drives without a position sensor part II: Adaptive methods. In *The XIX International Conference on Electrical Machines - ICEM 2010*, pages 1–6, Sep. 2010. DOI: 10.1109/ICELMACH.2010.5607980.

[BP08] A. Boglietti and M. Pastorelli. Induction and synchronous reluctance motors comparison. In *2008 34th Annual Conference of IEEE Industrial Electronics*, pages 2041–2044, Nov. 2008. DOI: 10.1109/IECON.2008.4758270.

[BPPS10] S. Bolognani, R. Petrella, A. Prearo, and L. Sgarbossa. On-line tracking of the MTPA trajectory in IPM motors via active power measurement. In *The XIX International Conference on Electrical Machines - ICEM 2010*, pages 1–7, Sep. 2010. DOI: 10.1109/ICELMACH.2010.5607843.

[BSL+10] S. Beineke, J. Schirmer, J. Lutz, H. Wertz, A. Bähr, and J. Kiel. Implementation and applications of sensorless control for synchronous machines in industrial inverters. In *2010 First Symposium on Sensorless Control for Electrical Drives*, pages 64–71, Jul. 2010. DOI: 10.1109/SLED.2010.5542802.

[CČerný10] Z. Caha and M. Černý. *Elektrické pohony*. SNTL, Praha, 2010.

[CM18] B. Carter and R. Mancini. *Op Amps for Everyone*. Newnes, 5 edition, 2018. DOI: 10.1016/B978-0-12-811648-7.15003-4.

[DTCB22] A. Dianov, F. Tinazzi, S. Calligaro, and S. Bolognani. Review and Classification of MTPA Control Algorithms for Synchronous Motors. *IEEE Transactions on Power Electronics*, 37(4):3990–4007, Apr. 2022. DOI: 10.1109/TPEL.2021.3123062.

[DW12] J. Dong and F. Wang. Study of analytical current ripple of three-phase PWM converter. In *2012 Twenty-Seventh Annual IEEE Applied Power Electronics Conference and Exposition (APEC)*, pages 1568–1575, Feb. 2012. DOI: 10.1109/APEC.2012.6166029.

[FZYJ20] G. Fengtao, Y. Zhonggang, Z. Yanping, and L. Jing. High Efficiency Sensorless Control of SynRM with Inductance Identification Based on Adaptive Alternate EKF. In *IECON 2020 The 46th Annual Conference of the IEEE Industrial Electronics Society*, pages 997–1002, Oct. 2020. DOI: 10.1109/IECON43393.2020.9254901.

[HKS99] J. Ha, S. Kang, and S. Sul. Position-controlled synchronous reluctance motor without rotational transducer. *IEEE Transactions on Industry Applications*, 35(6):1393–1398, Nov. 1999. DOI: 10.1109/28.806054.

[HNS17] M. Hofer, M. Nikowitz, and M. Schroedl. Sensorless control of a reluctance synchronous machine in the whole speed range without voltage pulse injections. In *2017 IEEE 3rd International Future Energy Electronics Conference and ECCE Asia (IFEEC 2017 - ECCE Asia)*, pages 1194–1198, Jun. 2017. DOI: 10.1109/IFEEC.2017.7992211.

[IKK+09] J. Im, W. Kim, K. Kim, C. Jin, J. Choi, and J. Lee. Inductance Calculation Method of Synchronous Reluctance Motor Including Iron Loss and Cross Magnetic Saturation. *IEEE Transactions on Magnetics*, 45(6):2803–2806, Jun. 2009. DOI: 10.1109/TMAG.2009.2018663.

[ITDO06] S. Ichikawa, M. Tomita, S. Doki, and S. Okuma. Sensorless Control of Synchronous Reluctance Motors Based on Extended EMF Models Considering Magnetic Saturation With Online Parameter Identification. *IEEE Transactions on Industry Applications*, 42(5):1264–1274, Sep. 2006. DOI: 10.1109/TIA.2006.880848.

[JSH+02] J. Jang, S. Sul, J. Ha, K. Ide, and M. Sawamura. Sensorless drive of SMPM motor by high frequency signal injection. In *APEC. Seventeenth Annual IEEE Applied Power Electronics Conference and Exposition (Cat. No.02CH37335)*, volume 1, pages 279–285, Mar. 2002. DOI: 10.1109/APEC.2002.989259.

[JZL+19] S. Jia, P. Zhang, D. Liang, M. Dai, and J. Liu. Design and Comparison of Three Different Types of IE4 Efficiency Machines. In *2019 22nd International Conference on Electrical Machines and Systems (ICEMS)*, pages 1–4, Aug. 2019. DOI: 10.1109/ICEMS.2019.8921786.

[KC17] A. Kumar and D. Chatterjee. A survey on space vector pulse width modulation technique for a two-level inverter. In *2017 National Power Electronics Conference (NPEC)*, pages 78–83, Dec. 2017. DOI: 10.1109/NPEC.2017.8310438.

[Kol10] J. Kolehmainen. Synchronous Reluctance Motor With Form Blocked Rotor. *IEEE Transactions on Energy Conversion*, 25(2):450–456, Jun. 2010. DOI: 10.1109/TEC.2009.2038579.

[Kos23] J. K. Kostko. Polyphase reaction synchronous motors. *Journal of the American Institute of Electrical Engineers*, 42(11):1162–1168, Nov. 1923. DOI: 10.1109/JoAIEE.1923.6591529.

[KS96] S. Kang and S. Sul. Highly dynamic torque control of synchronous reluctance motor. In *PESC Record. 27th Annual IEEE Power Electronics Specialists Conference*, volume 2, pages 1793–1797, Jun. 1996. DOI: 10.1109/PESC.1996.548824.

[KSG+14] S. Kondo, Y. Sato, T. Goto, M. Tomita, M. Hasegawa, S. Doki, and S. Kato. Position and velocity sensorless control for synchronous reluctance motor at low speeds and under loaded conditions using high-frequency extended EMF observer and heterodyne detection. In *2014 International Conference on Electrical Machines (ICEM)*, pages 857–863, Sep. 2014. DOI: 10.1109/ICELMACH.2014.6960281.

[LK19] X. Li and R. Kennel. Comparison of state-of-the-art estimators for electrical parameter identification of PMSM. In *2019 IEEE International Symposium on Predictive Control of Electrical Drives and Power Electronics (PRECEDE)*, pages 1–6, May 2019. DOI: 10.1109/PRECEDE.2019.8753197.

[MDD+22] M. Murataliyev, M. Degano, M. Di Nardo, N. Bianchi, and C. Gerada. Synchronous Reluctance Machines: A Comprehensive Review and Technology Comparison. *Proceedings of the IEEE*, 110(3):382–399, Jan. 2022. DOI: 10.1109/JPROC.2022.3145662.

[Moo96] T. K. Moon. The expectation-maximization algorithm. *IEEE Signal Processing Magazine*, 13(6):47–60, 1996. DOI: 10.1109/79.543975.

[NSS20] M. Nikowitz, R. Spiessberger, and M. Schroedl. Influence of the current sensor characteristics on the INFORM-method. In *PCIM Europe digital days 2020; International Exhibition and Conference for Power Electronics, Intelligent Motion, Renewable Energy and Energy Management*, 2020. ISBN: 978-3-8007-5245-4.

[ODM15] C. Oprea, A. Dziechciarz, and C. Martis. Comparative analysis of different synchronous reluctance motor topologies. In *2015 IEEE 15th International Conference on Environment and Electrical Engineering (EEEIC)*, pages 1904–1909, Jun. 2015. DOI: 10.1109/EEEIC.2015.7165463.

[QH13] Z. Qu and M. Hinkkanen. Loss-minimizing control of synchronous reluctance motors - A review. In *2013 IEEE International Conference on Industrial Technology (ICIT)*, pages 350–355, Feb. 2013. DOI: 10.1109/ICIT.2013.6505697.

[RFC10] M. Rajabi, M. Freddy, and S. Chandur. Theoretical and Experimental Reevaluation of Synchronous Reluctance Machine. *IEEE Transactions on Industrial Electronics*, 57(1):6–13, Jan. 2010. DOI: 10.1109/TIE.2009.2025286.

[RK20] P. Resutik and S. Kascak. Estimation of power losses and temperature distribution in three-phase inverter. In *2020 ELEKTRO*, pages 1–5, 2020. DOI: 10.1109/ELEKTRO49696.2020.9130255.

[RSW18] R. Raja, T. Sebastian, and M. Wang. Practical Implementation of Current Derivative Measurement for Sensorless Control of Permanent Magnet Machines. In *2018 IEEE Transportation Electrification Conference and Expo (ITEC)*, pages 1–6, Jun. 2018. DOI: 10.1109/ITEC.2018.8450148.

[RSW19] R. Raja, T. Sebastian, and M. Wang. Online stator inductance estimation for permanent magnet motors using PWM excitation. *IEEE Transactions on Transportation Electrification*, 5(1):107–117, Mar. 2019. DOI: 10.1109/TTE.2019.2891047.

[Sem12] ON Semiconductor. AN-9070 Smart Power Module Motion SPM® Products in SPM45H Packages. `<https://www.onsemi.com/pub/Collateral/AN-9070.pdf>`, Aug. 2012. Accessed: 2022-08-30.

[Sem14] ON Semiconductor. FNB41560/FNB41560B2 Motion SPM 45 Series Datasheet. `<https://www.onsemi.com/pdf/datasheet/fnb41560b2-d.pdf>`, Jan. 2014. Accessed: 2022-08-30.

[SKUU03] T. Senjyu, K. Kinjo, N. Urasaki, and K. Uezato. High efficiency control of synchronous reluctance motors using extended Kalman filter. *IEEE Transactions on Industrial Electronics*, 50(4):726–732, Aug. 2003. DOI: 10.1109/TIE.2003.814998.

[TH14] T. Tuovinen and M. Hinkkanen. Adaptive Full-Order Observer With High-Frequency Signal Injection for Synchronous Reluctance Motor Drives. *IEEE Journal of Emerging and Selected Topics in Power Electronics*, 2(2):181–189, Jun. 2014. DOI: 10.1109/JESTPE.2013.2294359.

[Tuo14] T. Tuovinen. *Model-Based Position Estimation for Synchronous Reluctance Motor Drives*. School of Electrical Engineering, Helsinki, 2014. ISBN: 978-952-60-5727-9.

[VPF96] A. Vagati, M. Pastorelli, and G. Franceschini. High performance control of synchronous reluctance motor. In *IAS '96. Conference Record of the 1996 IEEE Industry Applications Conference Thirty-First IAS Annual Meeting*, volume 1, pages 295–303, Oct. 1996. DOI: 10.1109/IAS.1996.557035.

[WB06] G. Welch and G. Bishop. *An Introduction to the Kalman Filter*. University of North Carolina at Chapel Hill, Chapel Hill, NC, USA, Jul. 2006.

[XXLN91] L. Xu, X. Xu, T. A. Lipo, and D. W. Novotny. Vector control of a synchronous reluctance motor including saturation and iron loss. *IEEE*

Transactions on Industry Applications, 27(5):977–985, Sep. 1991. DOI: 10.1109/28.90356.

[YAA09] S. Yamamoto, J. B. Adawey, and T. Ara. Maximum efficiency drives of synchronous reluctance motors by a novel loss minimization controller considering cross-magnetic saturation. In *2009 IEEE Energy Conversion Congress and Exposition*, pages 288–293, Sep. 2009. DOI: 10.1109/ECCE.2009.5316379.

ABSTRACT
Synchronous reluctance motors are becoming a more and more popular alternative to the AC induction machine for their relatively high power efficiency, low cost, and high robustness. Full utilization of benefits of sensorless control and high power efficiency are being complicated by non-linearities of the motor, especially magnetic saturation. The beginning of this work is dedicated to an inference of the mathematical-physical model of SynRM and an overview of existing state-of-the-art sensorless power-optimal algorithms. The core of this work is then the introduction of the SynRM state and parameter estimator, which is based on a new approach to measurement and utilization of phase reluctances. The key elements of the algorithm are a new methodology for measuring phase reluctances, a PWM switching scheme that allows to reduce switching losses and to measure phase reluctances from zero speed, and finally the integration of these measurements with the SynRM mathematical model using extended Kalman filter. The experimental part of the thesis then discusses the real measurement results obtained with the proposed algorithms and several selected state-of-the-art algorithms.

ABSTRAKT
Synchronní reluktanční motory se pro svou relativně vysokou účinnost, robustnost a nízkou cenu stávají stále populárnější alternativou velmi rozšířených asynchronních motorů. Snaha o využití výhodných vlastností bezsnímačového řízení, a dosažení co nejvyšší účinnost jejich provozu, je však komplikována jejich výraznou nelinearitou způsobenou saturací magnetického obvodu. Úvod této práce je věnován popisu matematicko-fyzikálního modelu SynRM a přehledu existujících moderních algoritmů výkonově-optimálního bezsnímačového řízení. Jádrem práce je pak představení estimátoru stavů a parameterů SynRM postaveného na novém přístupu k měření a využití fázových reluktancí. Klíčovými prvky algoritmu jsou nová metodologie měření fázových reluktancí, spínací PWM schéma jež umožňuje snížit spínací ztráty a měřit fázové reluktance od nulových otáček, a nakonec integrace těchto měření s matematickým modelem SynRM s pomocí rozšířeného Kalmánova filtru. Experimentální část práce pak diskutuje výsledky reálných měření s navrženým algoritmem a vybranými současnými algoritmy.